

Climatology of the CO vertical distribution on Mars based on ACS TGO measurements

Anna A. Fedorova¹, Alexander Trokhimovskiy², Franck Lefèvre³, Kevin S. Olsen⁴, Oleg I Korablev², Franck Montmessin⁵, Nikolay I. Ignatiev⁶, Alexander A Lomakin², Francois Forget⁷, Denis A. Belyaev², Juan Alday⁸, Mikhail Luginin¹, Andrey Patrakeev¹, Alexey V. Shakun², and Alexey Grigoriev¹

¹Space Research Institute

²Space Research Institute (IKI)

³LATMOS

⁴University of Oxford

⁵LATMOS CNRS/UVSQ/IPSL

⁶Space Research Institute of Russian Academy of Sciences

⁷Laboratoire de Meteorologie Dynamique

⁸Open University

November 21, 2022

Abstract

Carbon monoxide is a non-condensable species of the Martian atmosphere produced by the photolysis of CO₂. Its mixing ratio responds to the condensation and sublimation of CO₂; from the polar caps, resulting in seasonal variations of the CO abundance. Since 2018, all three spectrometers of the Atmospheric Chemistry Suite (ACS) onboard the Trace Gas Orbiter have measured CO in infrared bands by solar occultation. Here we provide the first long-term monitoring of the CO vertical distribution at the altitude range from 0 to 80 km for 1.5 Martian years from Ls=163; of MY34 to the end of MY35. We obtained a mean CO volume mixing ratio of ~960 ppm at latitudes from 45S to 45N, mostly consistent with previous observations. We found a strong enrichment of CO near the surface at Ls=100-200; in high southern latitudes with a layer of 3000-4000 ppmv, corresponding to local depletion of CO₂. At equinoxes we found an increase of mixing ratio above 50 km to 3000-4000 ppmv explained by the downwelling flux of the Hadley circulation on Mars, which drags the CO enriched air. The general circulation chemical model tends to overestimate the intensity of this process, bringing too much CO. The observed minimum of CO in the high and mid-latitudes southern summer atmosphere amounts to 700-750 ppmv, agreeing with nadir measurements. During the global dust storm of MY34, when the H₂O abundance peaks, we see less CO than during the calm MY35, suggesting an impact of HOx chemistry on the CO abundance.



Journal of Geophysical Research - planets

Supporting Information for

Climatology of the CO vertical distribution on Mars based on ACS TGO measurements

Anna Fedorova¹, Alexander Trokhimovskiy¹, Franck Lefèvre², Kevin S. Olsen³, Oleg Korablev¹, Franck Montmessin², Nikolay Ignatiev¹, Alexander Lomakin¹, Francois Forget⁴, Denis Belyaev¹, Juan Alday^{3,5}, Mikhail Luginin¹, Andrey Patrakeev¹, Alexey Shakun¹ & Alexey Grigoriev^{1,6}

¹Space Research Institute (IKI) RAS, Moscow, Russian Federation.

²LATMOS, CNRS, Sorbonne Université, Université Versailles Saint-Quentin-en-Yvelines, Guyancourt, France.

³Department of Physics, University of Oxford, Oxford, UK.

⁴Laboratoire de Météorologie Dynamique, Sorbonne Université, Centre National de la Recherche Scientifique, Jussieu, Paris, France

⁵School of Physical Sciences, The Open University, Milton Keynes, UK

⁶Australian National University, Research School of Astronomy and Astrophysics, Mount Stromlo Observatory, Advanced Instrumentation and Technology Centre, Canberra, Australia

Contents of this file

Text S1 to S2 Figures S1 to S7

Introduction

Supporting information file contains the validation of CO mixing ratio measurements between ACS experiments and additional figure with water vapor difference between MY34 and MY35 at Ls=180-240 for Section 3.6):

S.1 Validation of CO measurements between the ACS channels

From the beginning of Exomars TGO science program in 2018 the simultaneous observations of the same gases by TGO spectrometers allowed us to validate measurements and methods. It was done firstly for comparison of temperature and CO₂ density profiles retrieved by ACS NIR and MIR in different CO bands (Alday et al., 2019; 2021; Fedorova et al., 2020).

S.1.1 Validation of NIR by TIRVIM

There are two CO bands within the TIRVIM spectral range: 2.3 μm (transition 2-0) and 4.7 μm (transition 1-0). The signal-to-noise ratio of TIRVIM is 90–100 for pure Sun in the 4.7- μm range to ~ 150 at 2.3 μm . An example of TIRVIM spectra recorded during one occultation are shown at Figure S1. Despite the 4.7 μm spectral range being characterized by lower SNR compared to 2.3 μm , the fundamental 1-0 band is much stronger than 2-0 overtone (Fig. S1). We therefore used it to retrieve the CO vertical profiles based on the TIRVIM data.

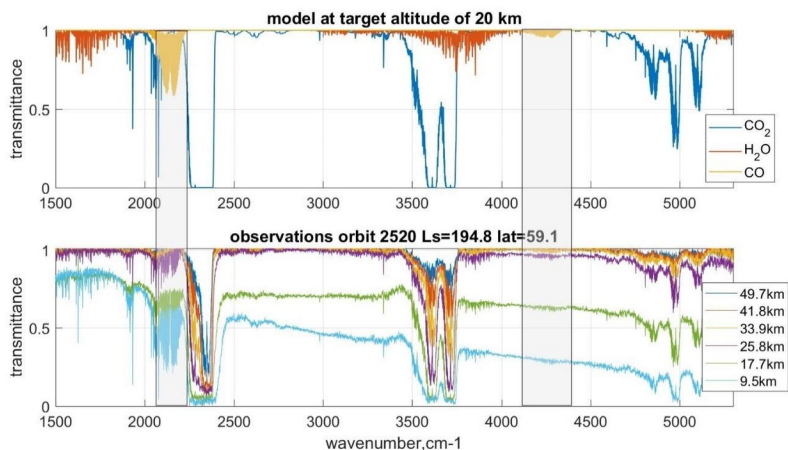


Figure S1. Example of transmittance spectra recorded by TIRVIM in solar occultation at orbit 2520 at different altitude in comparison with direct modeling at target altitude of 20 km for three main gases CO₂, H₂O and CO. Shaded areas show the range of CO 1-0 and 2-0 bands at 4.7 and 2.3 μm used for retrieval in this work.

TIRVIM stopped working in December 2019 (Ls=115° MY35) having recorded ~ 1000 solar occultations. We found about 550 co-located observations where the retrieval was done with NIR temperature profiles (Fig. S2). Overall, the profiles are well consistent in different locations and seasons (Fig. S3). However, the large FOV of TIRVIM ($\sim 2^\circ$ equal to ~ 60 km at the limb) makes the contribution of scattered light around the Sun close to the solar signal in the low atmosphere where the aerosol opacity reduces the signal. To make the valid retrieval of gaseous absorption in dusty condition the full radiative transfer with multiple scattering is needed, a difficult problem, given the poorly constrained FOV. We therefore limited the TIRVIM retrievals to transmittance of 0.6 (the aerosol slant optical depth of ~ 0.5).

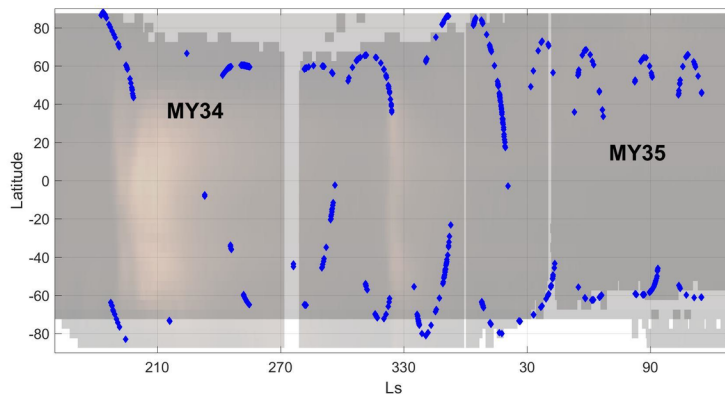


Figure S2. Collocated TIR-NIR observations for MY34-35 (2018-2019). The background is the distribution of dust optical depth for MY34 from Montabone et al., 2020.

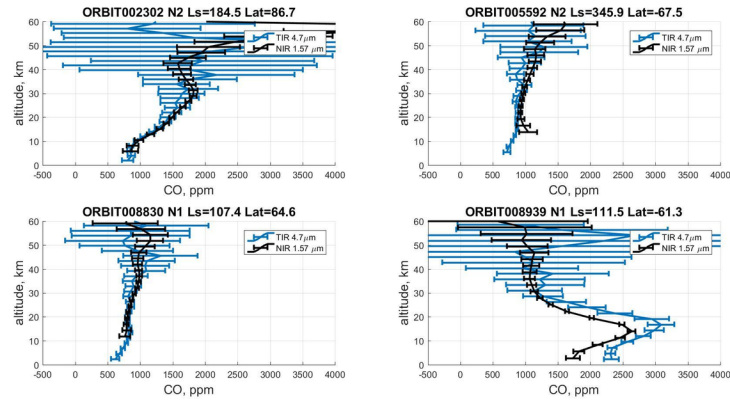


Figure S3. Examples of simultaneous observations of TIRVIM and NIR

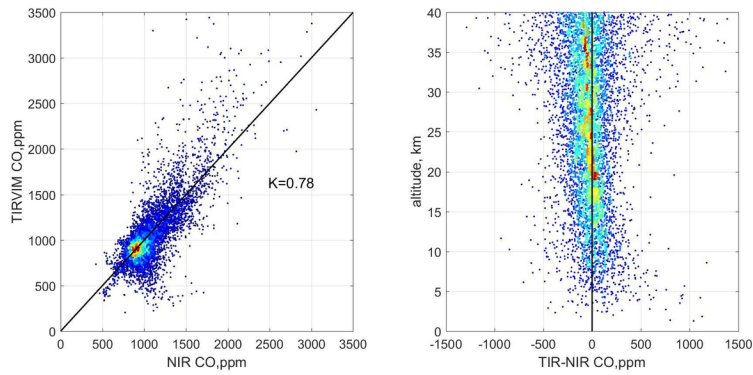


Figure S4. Validation of the retrieved vertical profiles of CO vmrs from ACS NIR and TIRVIM spectra for 550 co-located orbits, and the corresponding altitude distribution of the difference in the retrieved vmr. Blue-to-red color indicates the increasing density of points.

S.1.2 Validation of NIR with MIR

Nearly all measurements of ACS MIR were made simultaneously with ACS NIR. Figure S5 shows the difference of vmr values for simultaneous observations. It demonstrates good agreement between the two datasets, within 20% below 50 km.

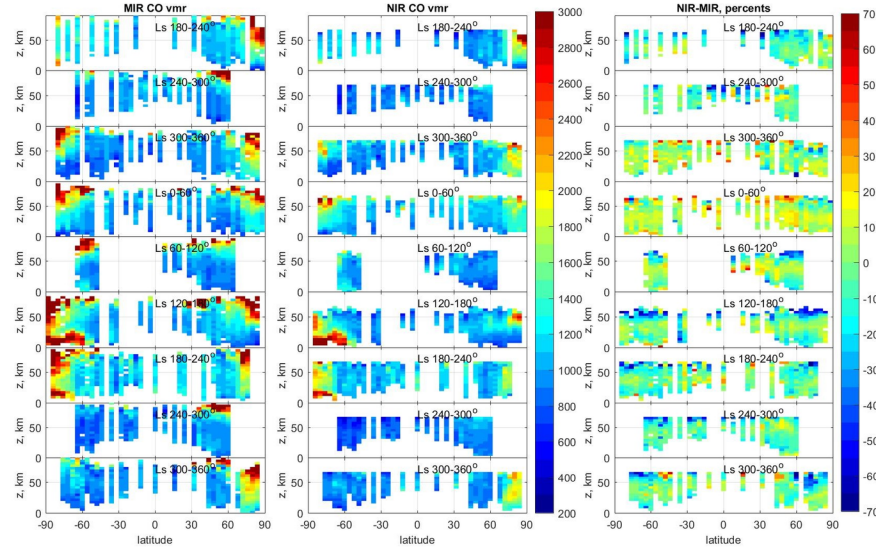


Figure S5. CO mixing ratio distribution of latitude and altitude for different Ls bins for simultaneous NIR and MIR orbits.

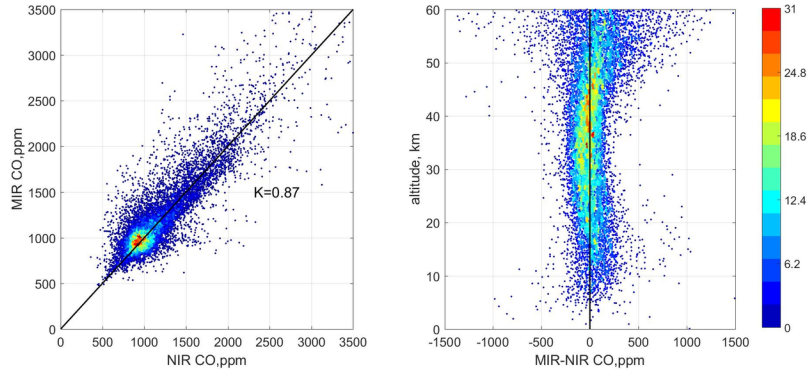


Figure S6. Correlation between CO vmrs retrieved from NIR and TIRVIM spectra for 600 co-located orbits, and the corresponding altitude distribution. Blue-to-red color indicates the increasing density of points.

S.2 Water variations during the Ls=180-240 in MY34 and MY35

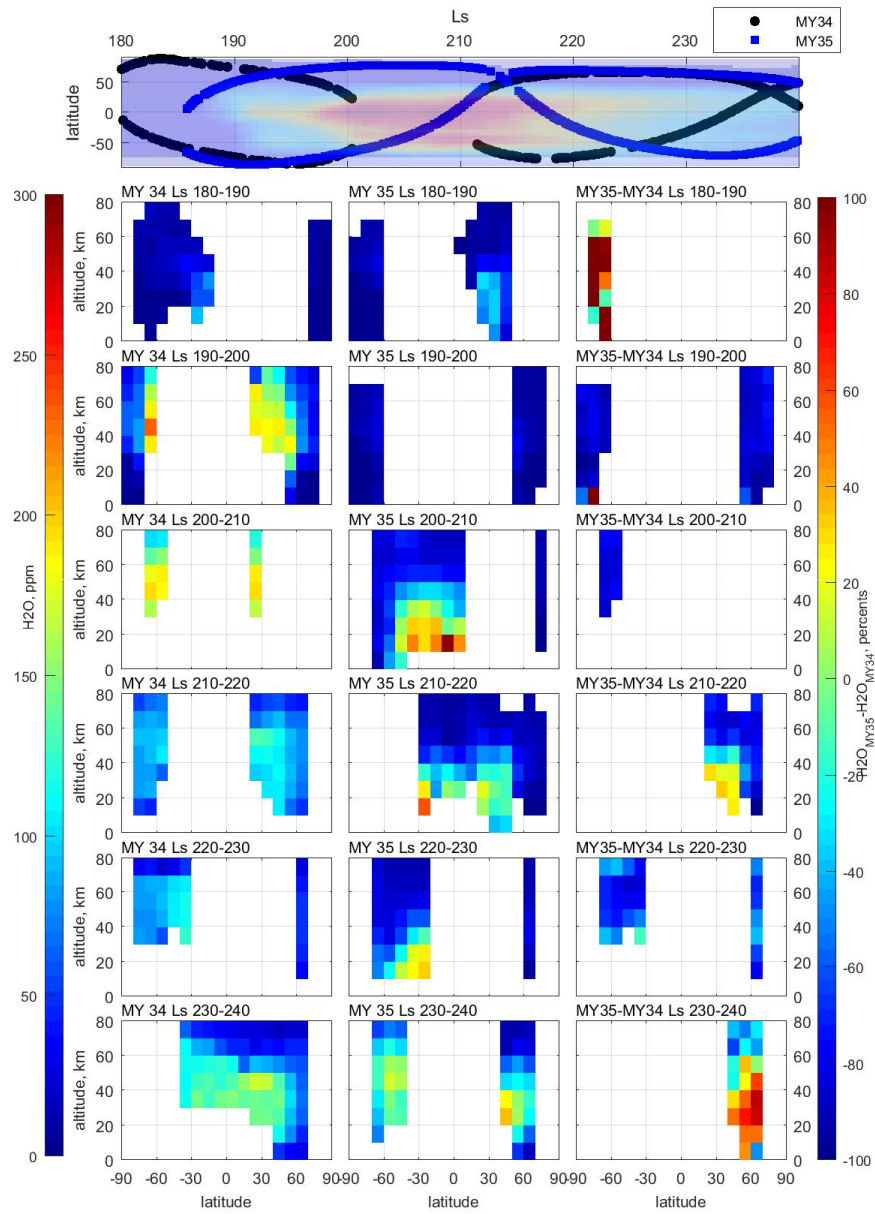


Figure S7. The latitudinal trend of the H_2O mixing ratio vertical profiles in ppmv into 10° Ls bins from $\text{Ls}=180^\circ$ to 240° for MY34 (left) and MY35 (middle) and relative difference in percent. On the top the seasonal distribution of ACS NIR solar occultation observation for MY 34 and 35 at $\text{Ls}=180\text{-}240^\circ$. The colored background is the dust optical depth distribution in $9\ \mu\text{m}$ for MY 34 from Montabone et al. (2020) with red color corresponding to maximal optical depth and blue color corresponding to minimal.

- 24 • Strong enrichment of CO, >3000 ppmv, is detected at 10-20 km at Ls=100-200 in
25 high southern latitudes and above 50 km at equinoxes near Poles.

26 **Abstract**

27 Carbon monoxide is a non-condensable species of the Martian atmosphere produced by the
28 photolysis of CO₂. Its mixing ratio responds to the condensation and sublimation of CO₂ from the
29 polar caps, resulting in seasonal variations of the CO abundance. Since 2018, all three
30 spectrometers of the Atmospheric Chemistry Suite (ACS) onboard the Trace Gas Orbiter have
31 measured CO in infrared bands by solar occultation. Here we provide the first long-term
32 monitoring of the CO vertical distribution at the altitude range from 0 to 80 km for 1.5 Martian
33 years from Ls=163° of MY34 to the end of MY35. We obtained a mean CO volume mixing ratio
34 of ~960 ppm at latitudes from 45°S to 45°N, mostly consistent with previous observations. We
35 found a strong enrichment of CO near the surface at Ls=100-200° in high southern latitudes with
36 a layer of 3000-4000 ppmv, corresponding to local depletion of CO₂. At equinoxes we found an
37 increase of mixing ratio above 50 km to 3000–4000 ppmv explained by the downwelling flux of
38 the Hadley circulation on Mars, which drags the CO enriched air. The general circulation chemical
39 model tends to overestimate the intensity of this process, bringing too much CO. The observed
40 minimum of CO in the high and mid-latitudes southern summer atmosphere amounts to 700-750
41 ppmv, agreeing with nadir measurements. During the global dust storm of MY34, when the H₂O
42 abundance peaks, we see less CO than during the calm MY35, suggesting an impact of HO_x
43 chemistry on the CO abundance.

44 **Plain language summary**

45 Carbon monoxide (CO) is a product of the photolysis of the main component of the Martian
46 atmosphere, CO₂ (96%). During the polar night on Mars, the temperature drops so low that ~30%
47 of the global atmospheric carbon dioxide freezes out, condensed into snowflakes. They settle to
48 the ground to form a seasonal polar cap, which sublimates in spring after. Unlike CO₂, CO is not
49 a condensable species, so its relative abundance increases when CO₂ and the atmospheric pressure

50 drops, forming a prominent seasonal cycle. This behaviour of CO was well documented by nadir
51 spacecraft observations, while its vertical distribution remained a white spot until recently. Still, it
52 helps to separate the impact of photolysis and the atmospheric dynamics, addressing the problem
53 of the Martian atmosphere's stability. We present the first climatology of the CO vertical
54 distribution lasting more than one Martian year based on solar occultation by the Trace Gas
55 Orbiter. We report a previously unobserved CO layer near the surface in high southern latitudes in
56 late winter and spring and document the difference between MY34 and MY35 caused by the global
57 dust storm. These observations give new challenges to the Martian GCMs for understanding the
58 modern atmosphere of Mars.

59

60 **1. Introduction**

61 Carbon monoxide (CO) is produced by the photolysis of CO₂ and plays a crucial role in
62 the photochemical cycle that stabilizes the atmosphere's composition. CO was discovered by
63 [Kaplan et al. \(1969\)](#). Its observed abundance is by two orders of magnitude lower than the expected
64 abundance of ~8% in the context of a dry atmosphere ([Nair et al., 1994](#)). This inconsistency posed
65 a problem of the stability of CO₂ in the Martian atmosphere, later resolved by introducing catalytic
66 reactions with the H₂O photolysis products (like OH) (McElroy and Donahue (1972); Parkinson
67 and Hunten (1972)). Still, a problem persists in quantitative understanding of the HO_x chemistry
68 because current models mostly underestimate the amount of CO on Mars several times (Lefèvre
69 & Krasnopolsky, 2017).

70 The CO abundance on Mars has been measured by high-resolution ground-based
71 spectroscopy from infrared lines located in the 3-0 (1.57 μm, [Krasnopolsky, 2003](#); [Krasnopolsky,](#)
72 [2007](#)), 2-0 (2.3 μm, [Krasnopolsky, 2015](#); [Billebaud et al., 1998](#)) and 1-0 (4.7 μm, [Billebaud et al.,](#)
73 [1992](#)) bands of CO and rotational microwave spectrum ([Clancy et al., 1990](#); [Lellouch et al.,](#)
74 [1991](#)). The column-averaged CO mixing ratios inferred from these observations represented
75 mostly the abundance in the lower atmosphere. It varied from 600±150 ppmv (parts per million

76 by volume) to 800 ± 200 ppmv. Krasnopolsky et al. (2003) first reported the north-south asymmetry
77 of the CO distribution at $L_s = 112^\circ$ with CO volume mixing ratios (VMRs) varying from 830 ppmv
78 in the northern middle latitudes to 1250 ppmv at 50°S . The first map of CO abundance based on
79 several latitudinal tracks (Krasnopolsky 2007) showed an increase of CO abundance up to 1600
80 ppmv at $L_s = 112\text{--}173^\circ$.

81 The first CO seasonal distribution has been obtained from the nadir observations made by
82 OMEGA (Observatoire pour la Minéralogie, l'Eau, les Glaces et l'Activité) and PFS (Planetary
83 Fourier Spectrometer) onboard the Mars Express mission ([Encrenaz et al., 2006](#); [Billebaud et al.,](#)
84 [2009](#); [Sindoni et al., 2011](#); [Bouche et al., 2019; 2021](#)), CRISM (Compact Reconnaissance Imaging
85 Spectrometer for Mars) on board the Mars Reconnaissance Orbiter ([Smith et al., 2009, 2018](#)) and
86 recently NOMAD (Nadir and Occultation for Mars Discovery) onboard the Trace Gas Orbiter
87 (TGO) ([Smith et al., 2021](#)) using the $2.3 \mu\text{m}$ (2-0) and $4.7 \mu\text{m}$ (1-0) absorption bands. These
88 observations have shown strong seasonal variations of CO, especially in high latitudes. The
89 minimal values (down to 200 ppmv based on CRISM) have been found in the southern summer
90 high latitudes. At low-to-mid latitudes, the CO_2 condensation-sublimation cycle leads to a broad
91 peak at about $L_s = 180^\circ$ (evident in the models and CRISM, less so in NOMAD). The maximum
92 column-integrated mixing ratio (~ 1300 ppmv) was observed in low-to-mid latitudes around the
93 northern autumnal equinox about $L_s = 180^\circ$ as a result of the transport of the CO enriched air from
94 the winter polar region. CO behaves as other non-condensable gases like N_2 , Ar, O_2 , expected to
95 vary in response to the condensation-sublimation cycle of CO_2 into and from the seasonal polar
96 caps. Seasonal variations of argon were measured by Mars Odyssey gamma-ray spectrometer
97 ([Sprague et al., 2004; 2012](#)); similarly, variations of Ar, N_2 , O_2 and CO were found at the surface
98 by Sample Analysis at Mars (SAM) onboard the Curiosity rover (Trainer et al., 2019). This
99 phenomenon is well reproduced by general circulation model (GCM) simulations ([Forget et al.,](#)
100 [2008](#); Smith et al., 2018; [Holmes et al., 2019](#)).

101 The annual mean value of CO remains a topic of debate. Nadir measurements from PFS,
102 CRISM and NOMAD support a global average of ~800 ppmv (Bouche et al., 2021, Smith et al.,
103 2018, 2021). Earth-based observations yielded a lower value of ~700 ppmv (Krasnopolsky 2015).
104 In situ measurements by SAM/Curiosity resulted in an even lower value of 580 ppmv (Trainer et
105 al., 2019). After several Martian years of observations, such small mixing ratios were never
106 confirmed from orbit at the MSL location (Smith et al., 2018, 2021).

107 While the global seasonal trends of the CO column are relatively well understood, its
108 vertical distribution was poorly documented before the arrival of TGO at Mars. Using PFS, Bouche
109 et al. (2019; 2021) retrieved CO abundances by exploiting the vertical sensitivity of the 4.7 μm
110 band. These measurements carry information mainly on the CO column below 15 km with
111 enhanced sensitivity near the surface. However, their inferred vertical gradients at 0–20 km can
112 not be reproduced by 3D climate models, which rely on our current understanding of Martian
113 photochemistry (Forget et al., 2008). It made the authors attribute the observed vertical gradient
114 to the method artefact.

115 In 2018, the ExoMars TGO began its science phase by observing Mars' atmosphere from
116 its orbit. Two scientific instruments onboard TGO, the Atmospheric Chemistry Suite (ACS)
117 (Korablev et al., 2018) and NOMAD (Vandaele et al., 2018), can sound the vertical structure of
118 the atmosphere in solar occultation mode. ACS includes three high-resolution infrared
119 spectrometers: NIR (near-infrared), MIR (middle infrared) and TIRVIM (thermal infrared)
120 (Korablev et al., 2018). All three channels measure the vertical distribution of CO in three
121 spectroscopic bands used previously in ground-based and spacecraft observations: 1.57 μm (NIR),
122 2.3 μm (MIR and TIRVIM) and 4.7 μm (TIRVIM). The first CO vertical profiles were inferred
123 from ACS MIR at altitudes 20–120 km and $L_s=164\text{--}220^\circ$ before and during the global dust storm
124 (GDS) of Mars year (MY) 34. They showed a prominent depletion in the CO mixing ratio up to
125 100 km, pointing to the importance of CO oxidation during wetter GDS conditions (Olsen et al.,
126 2021).

127 Here, we report the first long-term observations of the CO vertical distribution on Mars.
128 They are based primarily on the ACS NIR dataset and compared to ACS MIR and TIRVIM solar
129 occultation. We study the seasonal and latitudinal variations of the CO profiles for MY 34 and 35,
130 focusing on the interannual variability, and compare our data with the LMD Global Climate Model
131 results, including photochemistry (Lefèvre et al., 2004).

132 **2. Measurements and the CO retrievals**

133 **2.1 Dataset**

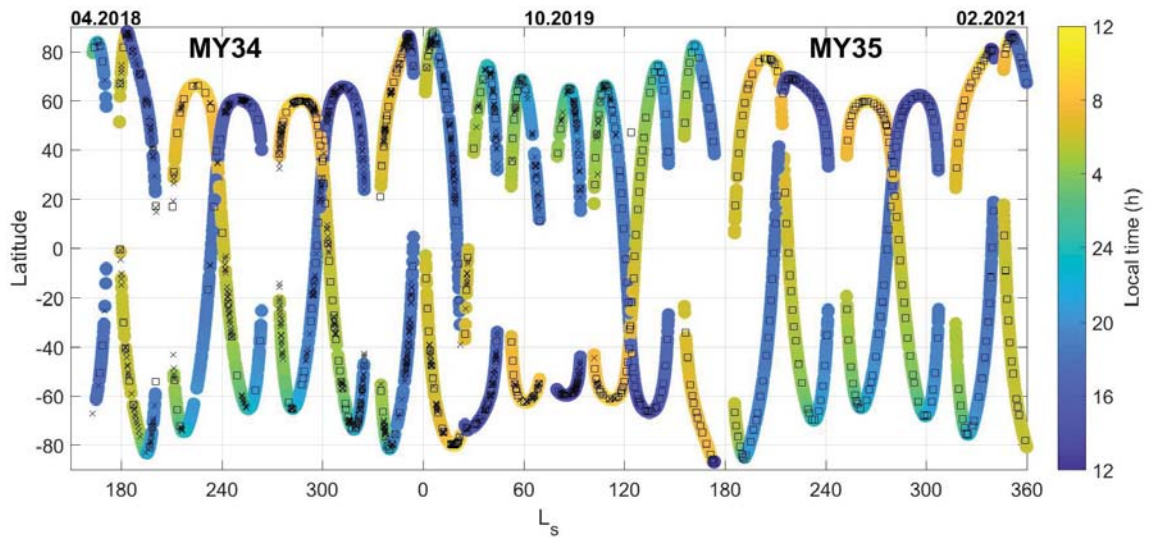
134 ACS is a dedicated solar occultation experiment, with all three channels operating in this
135 mode. In solar occultation, the transmittance at different altitudes in the atmosphere is derived by
136 rationing spectra with the reference solar spectrum obtained (before)after a (de)occultation when
137 observing the Sun outside the atmosphere. The method provides high sensitivity since the airmass
138 factor at the limb is ten times greater than in nadir, and the Sun is the brightest source of the Solar
139 system. The polar and circular orbit of the spacecraft (78° of inclination, 2 hours period and 400
140 km above the surface of the planet) was optimized to provide vertical profiling at unprecedented
141 spatial and temporal resolution (up to 24 occultations per day). The misalignment between ACS
142 MIR and NOMAD lines-of-sight (LOS) does not allow simultaneous measurements of all
143 occultation experiments onboard TGO. Thus, the number of occultations had to be divided
144 between NOMAD and ACS. However, the field-of-view (FOV) of NIR and TIRVIM allow
145 measurements with NOMAD pointing that result in different coverage and fullness of datasets for
146 three ACS spectrometers.

147 The densest dataset, which constitutes the basis of this study, was produced by ACS NIR,
148 which provides CO measurements in the $1.57\ \mu\text{m}$ band at 0-60 km for each occultation. From the
149 beginning of the TGO science phase in April 2018 ($L_s=163^\circ$ of MY34) to January 2021 ($L_s=360^\circ$
150 of MY35), ACS NIR collected about 6050 profiles (Figure 1). ACS NIR can use both kinds of
151 pointing (ACS-driven and NOMAD-driven), and we analysed occultation profiles obtained with
152 ACS and NOMAD pointing (the latter constituting $\sim 40\%$ of profiles).

153 ACS MIR gives access to a much stronger band of CO located at 2.35 μm , resulting in the
154 capability to measure CO up to 90–110 km. The MIR dataset includes 620 occultations performed
155 using secondary grating position 6 (see section 2.3). The validity of the NIR and MIR profiles was
156 established by comparing the two sets of profiles.

157 ACS TIRVIM measures both the 2.35 μm band and the strongest fundamental 4.7 μm band.
158 The interferogram can be obtained at high or low resolution observation mode defined by the
159 maximum optical path difference (MOPD). The MOPD of the TIRVIM interferometer can be as
160 large as 5 cm^{-1} . In the high-resolution mode (MOPD = 4.3 cm), the spectral sampling $\Delta\nu$ and the
161 spectral resolution (full width at half maximum of the instrumental function, FWHM, with
162 Hamming apodization) are equal to 0.11 and 0.21 cm^{-1} , respectively. In the low resolution mode
163 MOPD = 0.97 cm, $\Delta\nu = 0.51 \text{ cm}^{-1}$ and FWHM = 0.94 cm^{-1} . The largest part of occultations was
164 done in the low resolution mode and only 20 orbits with high resolution but with worse signal-to-
165 noise ratio (SNR). For the analysis, we used the low resolution mode TIRVIM observations of the
166 4.7 μm band to validate NIR and MIR results at 0–40 km. TIRVIM ceased operations in December
167 2019 (Ls=115° MY 35) after having recorded ~1000 solar occultations since the beginning of the
168 mission.

169 The following sections describe the datasets and the processing of ACS MIR, TIRVIM and
170 NIR, and introduce the validation of the retrieved CO profiles. An in-depth comparison of CO
171 VMRs retrieved from different channels can be found in Supplementary Material.



172

173 Figure 1. Observational coverage of ACS solar occultations. The color circles, where colours
 174 indicate the local time of the occultation, show NIR observations. Black squares show MIR
 175 observations of CO, and black crosses show TIRVIM observations.

176

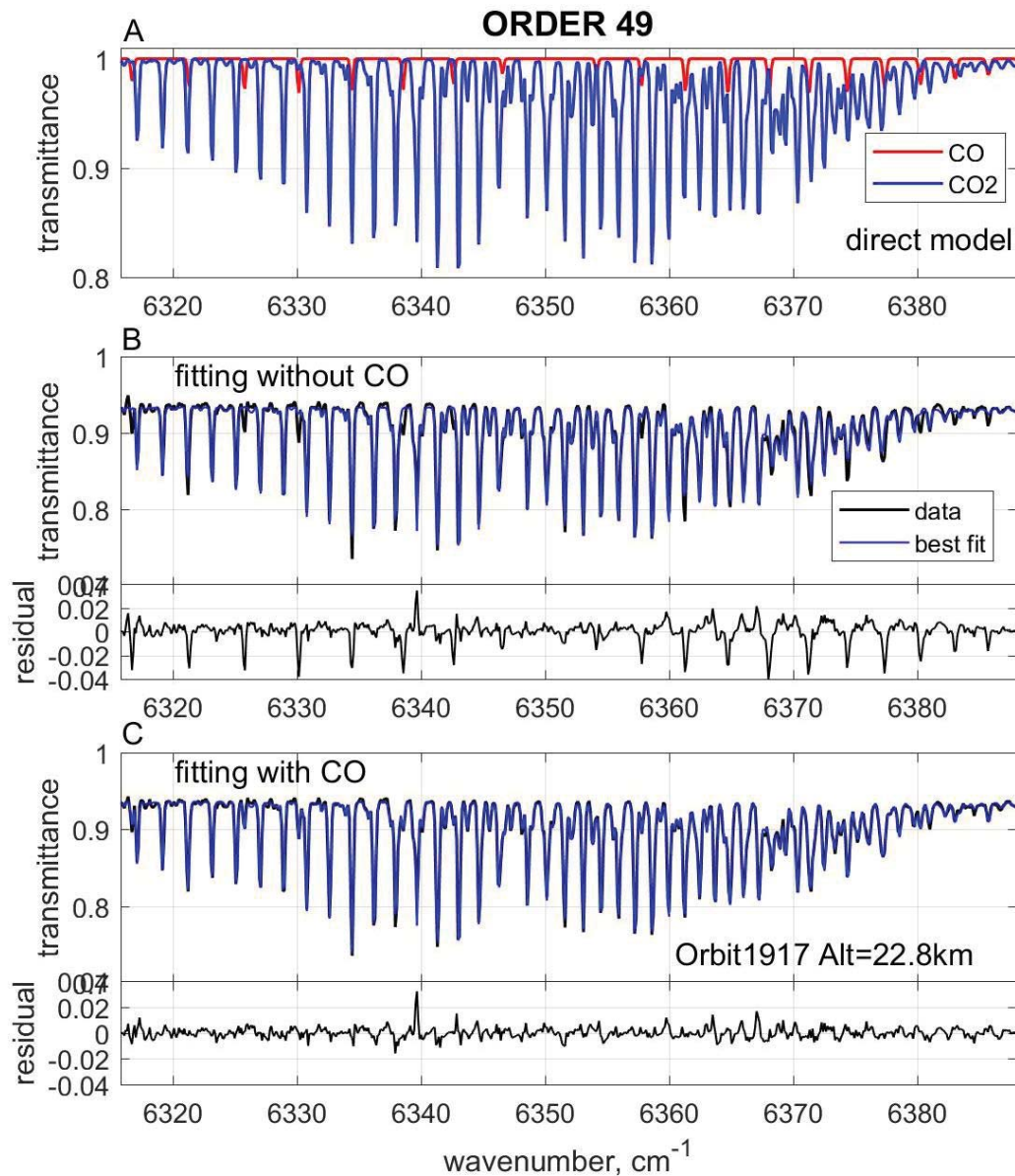
177 2.2 NIR

178 ACS NIR combines an acousto-optical tunable filter (AOTF), used as a monochromator that
 179 can be commanded to isolate a specific wavelength bandpass whose width corresponds to the free
 180 spectral range of the echelle grating that operates at high diffraction orders. It covers the 0.7–1.7
 181 μm spectral range using diffraction orders 101 through 49 (Trokhimovskiy et al., 2015a; Korablev
 182 et al., 2018). During an occultation, ACS NIR measures ten pre-selected diffraction orders every
 183 2 s, including the absorption bands of H_2O and CO_2 .

184 The instantaneous FOV in the direction perpendicular to the limb is small ($\sim 0.02^\circ$) and
 185 limited by the slit width. The FOV corresponds to an instantaneous vertical resolution of 500–600
 186 m at the tangent altitude of the line of sight. The time to measure one diffraction order is 0.2 s. The
 187 effective vertical resolution depends on the β -angle (the angle between the orbit plane and the
 188 direction to the Sun). It is generally better than 1 km for each diffraction order. Horizontal
 189 resolution (along the slit) is 1.5–5 km and is determined by the number of stacked detector lines.
 190 The number of detector lines measured in a single occultation and its position on the detector

191 depends on the pointing direction (NOMAD and ACS MIR-driven) and the available downlink
192 volume. It varies from 6 to 30 lines; the solar image size on the detector limits the upper boundary.
193 Averaging 30 detector lines does not worsen vertical resolution since that dimension of FOV is
194 oriented along the limb. The SNR for an individual pixel and pure solar signal in the AOTF
195 maximum equals about ~ 600 for the MIR pointing and ~ 300 for the NOMAD pointing. We
196 averaged 6–25 lines with the maximal signal, excluding the solar image edges, resulting in an SNR
197 of 800–3000, depending on the occultation.

198 Diffraction order 49 ($6318\text{--}6387\text{ cm}^{-1}$) was initially used to retrieve the temperature and CO₂
199 density using the $1.57\text{ }\mu\text{m}$ CO₂ band. This order also contains a weaker overlapping CO band.
200 Even if hardly noticeable within the strong CO₂ band, the retrieval algorithm detects the CO lines
201 well thanks to their periodic structure. It permits measuring the CO mixing ratio from 0 to 60-70
202 km. Figure 2 shows examples of spectra fitting in order 49 with and without CO. The $1.57\text{ }\mu\text{m}$
203 band was already used for measuring CO abundance in the Martian atmosphere using high-
204 resolution ground-based observations (Krasnopolsky, 2003).



205

206 Figure 2. Example of ACS NIR spectrum measured in order 49 at 23 km altitude showing

207 the benefit of fitting with a model including both CO₂ and CO. A): a synthetic model of CO₂ (blue)

208 and CO (red, 1000 ppmv) absorption bands. B): spectrum observed (in black) at orbit 1917,

209 L_s=167°, the latitude of 82°, east longitude of -92.3° and local time 21:15 with its best fit (in

210 blue) without CO and fit residual; (C) the same observed spectrum with its best fit (in blue) with

211 CO and fit residual.

212 The retrieval algorithm is based on a Levenberg–Marquardt iterative scheme and Tikhonov

213 regularization to smooth the profile and minimize the uncertainties. A forward transmission model

214 is computed using a look-up table of absorption cross-sections (as a function of pressure and
215 temperature) for a corresponding number of atmospheric layers (40 to 130 depending on orbit).
216 The spectral line parameters for the CO₂ and CO are taken from the HITRAN 2016 database
217 (Gordon et al., 2017) with CO₂-broadening coefficients for CO (Li et al., 2015) and self-
218 broadening for CO₂. The inverse problem is divided into two steps. The first step includes fitting
219 for temperature, pressure and CO mixing ratio based on the shape of the spectra only. In the second
220 step, we assume hydrostatic equilibrium to constrain the retrieval of temperature and pressure
221 simultaneously. We define a pressure P_0 at an altitude level z_0 where the uncertainties are minimal
222 (the highest data quality), and then compute the pressure profile from the hydrostatic equilibrium,
223 integrating the retrieved T profile above and below the P_0 level:

$$224 \quad P(h) = P_0 \exp\left(-\int_{z_0}^h \frac{g(z)M(z)}{T(z)k} dz\right),$$

225 where $g(z)$ is the acceleration due to gravity, $M(z)$ is the molecular weight (taken from the
226 Mars Climate Database (MCD) v5.3, Forget et al., 1999, Millour et al., 2018), k is the Boltzmann
227 constant, z is the altitude, h is the altitude level of pressure P . Once the pressure is calculated, we
228 repeat the temperature retrieval with only two free parameters, temperature and CO vmr, and
229 perform several iterations until the pressure and temperature profiles converge.

230 The retrieval products from order 49 are the CO₂ density, atmospheric temperature and CO
231 mixing ratio, as shown in figure 5. The detailed retrieval algorithm is described in (Fedorova et
232 al., 2020).

233

234 **2.3 MIR**

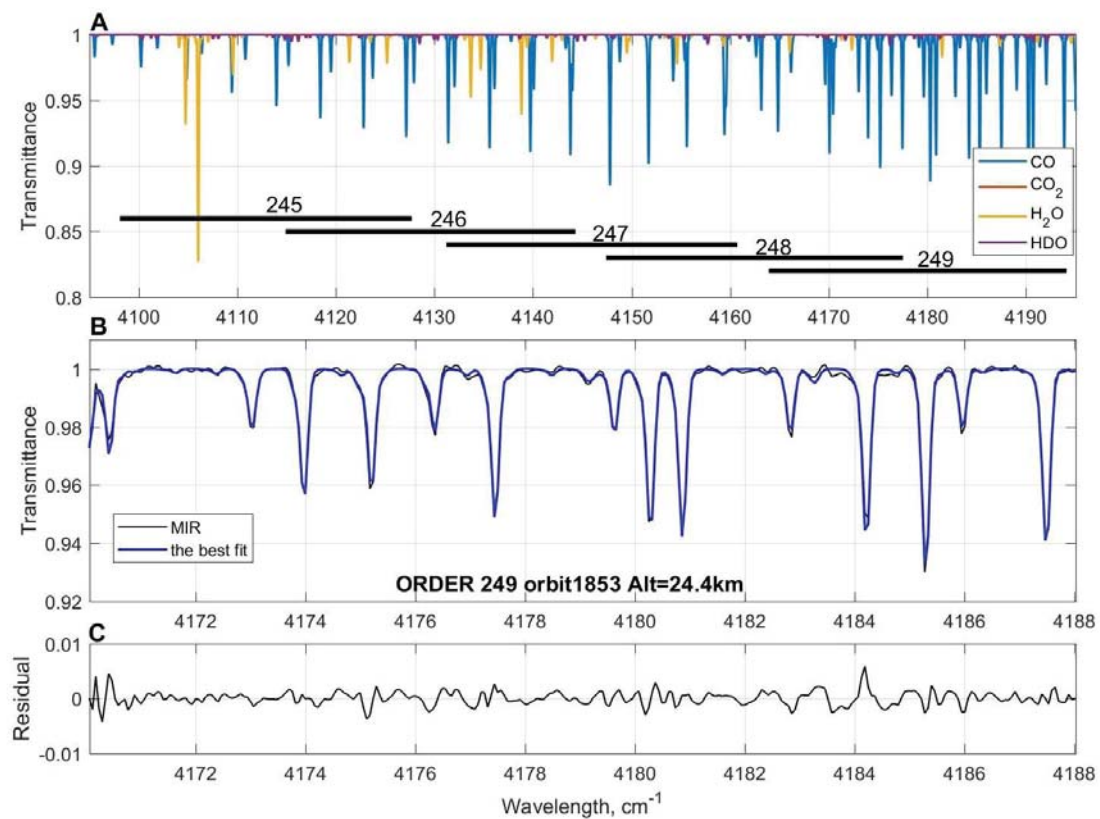
235 The ACS MIR (mid-infrared) channel is a crossed-dispersion echelle spectrometer dedicated
236 to solar occultation measurements in the 2.3–4.5 μm range with spectral resolving power of
237 $\sim 30,000$. The channel can only sample a fraction ($\sim 160 \text{ cm}^{-1}$) of the full range on a single
238 observation. To access a particular interval, a secondary dispersion grating is rotated to one of 11

239 positions (Korablev et al., 2018; Trokhimovskiy et al., 2015b, 2020). During an occultation, MIR
240 is operated in one pre-chosen secondary grating position. Spectra are recorded on a two-
241 dimensional detector, with the x -axis corresponding to wavenumber and the y -axis to diffraction
242 orders. MIR measures up to 20 adjacent diffraction orders for each acquired frame, covering an
243 instantaneous spectral range of 0.15–0.3 μm . Each diffraction order appears as a stripe over the
244 detector, covering around 20 rows. The stripe results from the vertical FOV, and each row is a
245 unique solar occultation spectrum separated by 100-200 m from its adjacent rows.

246 We use the strong 2.3 μm band for the CO retrieval, which can be measured in positions 6 or
247 7. Position 7 covers the strongest lines of the 2-0 transitions, located in orders 248–256, and allows
248 measuring CO abundances up to 110 km. Thirty-two ACS MIR occultations have been used to
249 assess the CO vertical distribution during the Global Dust Storm of MY 34 (Olsen et al., 2021). In
250 position 6, the three CO isotopes (main $\text{C}^{12}\text{O}^{16}$, $\text{C}^{13}\text{O}^{16}$, $\text{C}^{12}\text{O}^{18}$) are measured in orders 246-249
251 (Figure 3). Position 6 also contains CO_2 and H_2O absorption features, used as a reference in the
252 calibration pipeline, and CO monitoring was changed from position 7 to position 6 in November
253 2018. The line strengths are a little smaller than in Position 7, constraining the measurements of
254 CO up to 90 km. The strongest lines are found in order 249, used for the retrieval. The instrument
255 line shape is impacted by a doubling (or multiplying) of the image at the detector, originating from
256 an optical anomaly somewhere along the incidence optical path. As a result, many diffraction
257 orders display a doubling of absorption lines. The orders in the bottom part of the detector are
258 mostly free from this effect, and the lines in order 249 located in the lowest part of the detector
259 were preferable. Nevertheless, slight doubling was observed in order 249, and the instrumental
260 function was parameterized using a double gaussian with the fitting of its halfwidth and the relative
261 intensity of two maxima. These parameters are sought for each occultation. A similar approach
262 was described in Alday et al. (2019), Olsen et al. (2021) and Belyaev et al. (2021). The FOV of
263 MIR is small; its vertical resolution is mainly defined by the integration time and amounts to 2.5

264 km. We averaged ten detector lines near the stripe center for the retrieval, effectively increasing
265 the vertical resolution to 3 km.

266 The retrieval algorithm of CO from MIR data is similar to that described for the NIR channel.
267 Only two free parameter vectors are retrieved (the H₂O and CO VMRs). The CO₂ absorption band
268 in order 249 is weak and contributes only in the lower atmosphere and at low temperatures. We
269 fixed the CO₂ mixing ratio to 0.96 for the modeling. The HDO/H₂O ratio was assumed constant
270 and equal to 5 (Alday et al., 2021). The pressure and temperature profiles used for constraining
271 spectroscopic parameters are taken from the simultaneous NIR retrievals obtained for the same
272 occultation. The MIR CO vertical profiles for two orbits of MY 34 concurrent with NIR
273 observations are shown in Figure 5C, F.



274
275 Figure 3. An example ACS MIR spectrum measured in position 6 at 20 km altitude and the best
276 fit including CO, CO₂ and H₂O contributions. A) the direct model of CO, H₂O, CO₂ and HDO
277 absorption bands in orders 245-249 of position 6. B) spectrum observed at orbit 1853, Ls=164°,

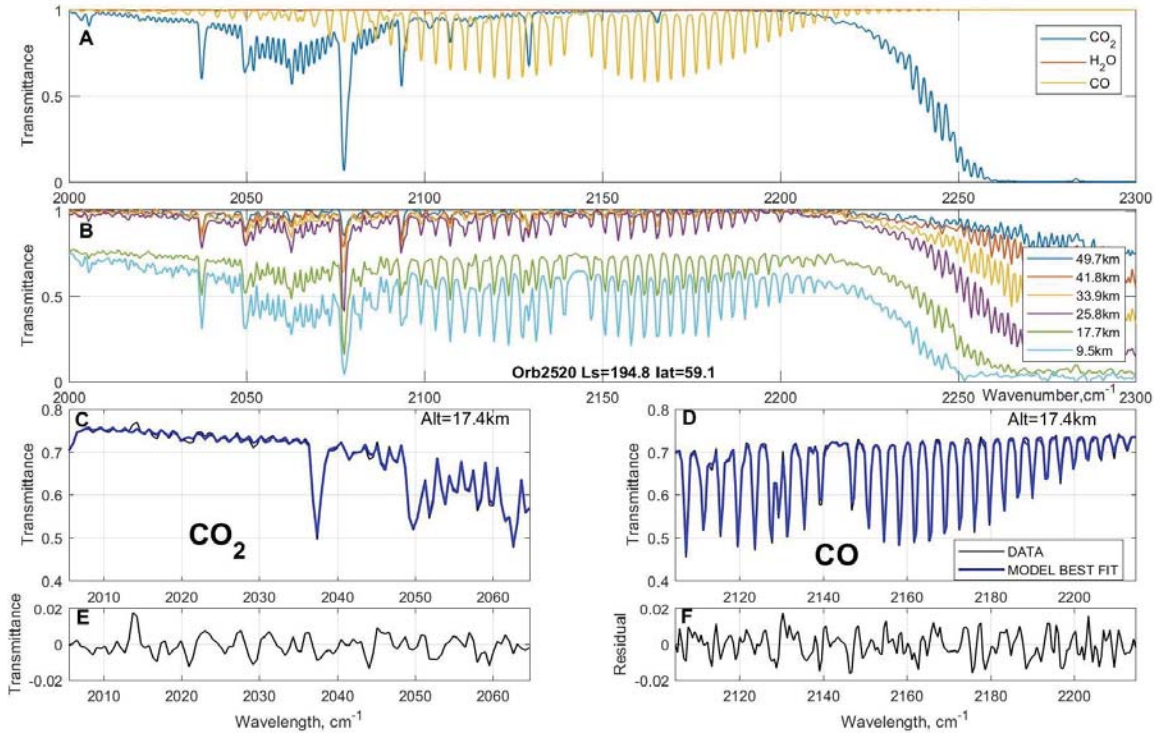
278 81.7°N, 20.5°E and local time of 02:20 (black curve) and the best fit of the data (blue curve); C)
279 residual for the spectrum.

280

281 **2.4 TIRVIM**

282 The thermal infrared (TIRVIM) channel is a Fourier transform spectrometer with solar
283 occultation capability (Korablev et al., 2018; Shakun et al., 2018). TIRVIM operates mainly in the
284 “climatology” mode in solar occultation geometry, covering the entire spectral range from 1.7 to
285 17 μm every 0.4 s, with a spectral resolution of 0.94 cm^{-1} . At 2.8° , the diameter of TIRVIM’s
286 circular FOV is larger than the solar disk. The vertical resolution, determined by the angular
287 diameter of the Sun, is close to one atmospheric scale height, varying with Sun-Mars distance from
288 8.8 to 10.6 km.

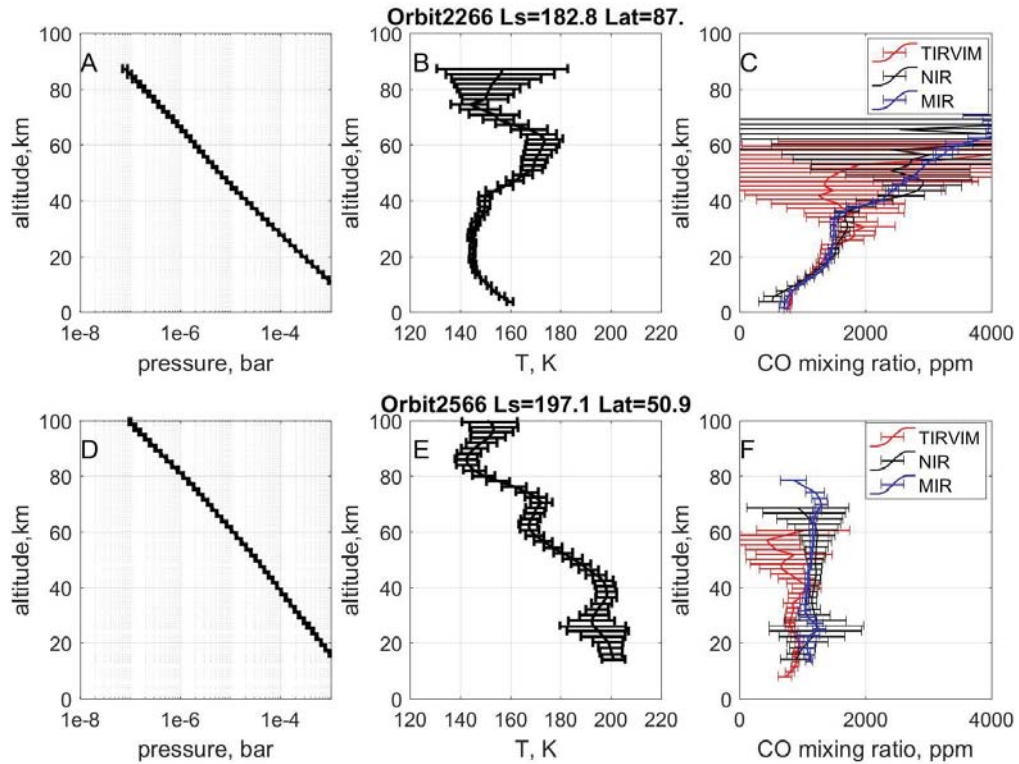
289 To retrieve CO from TIRVIM spectra, we used the strongest $4.7\text{ }\mu\text{m}$ band. The low SNR
290 (≤ 100 only) allows for vertical profile retrievals of CO below 50 km. To increase the SNR, four
291 consecutive spectra were averaged. The retrieval algorithm of CO from TIRVIM data is similar to
292 that described for the NIR and MIR channels. The temperature profiles are prescribed, retrieved
293 from coinciding NIR observations available for about half of TIRVIM occultations. For the
294 remaining observations, we used temperature profiles from the LMD GCM (Forget et al., 1999;
295 Montabone et al., 2020). The CO_2 density was retrieved from the nearby $4.9\text{ }\mu\text{m}$ CO_2 band. CO
296 VMRs were obtained as the ratio of CO and CO_2 densities. Examples of TIRVIM spectra and
297 fitting are presented in Figure 4, while CO VMR vertical profiles for two orbits in MY 34 are
298 shown in Figure 5C, F.



299

300 Figure 4. An example of measured ACS TIRVIM spectrum and its best fit showing the benefit of
 301 fitting with a model including both CO₂ and CO. A) the direct model of CO, H₂O, CO₂ absorption
 302 bands in the spectral range 2000-2300 cm⁻¹. B) spectra observed at different altitudes at orbit
 303 2520, Ls=194.8°, 60.2°N, 167°E and local time of 17:25; C, D) spectrum observed at 17 km at the
 304 same orbit 2520 (black curve) in the range of CO₂ and CO bands, respectively, and the best fit of
 305 the data (blue curve); F, E) residual for the spectrum of CO₂ and CO bands, respectively.

306



307

308 **Figure 5. Example profiles retrieved from ACS NIR-MIR-TIRVIM occultations.**

309 A) and D) pressure, derived from the CO₂ number density; B) and E) atmospheric temperature; C)
 310 and F) CO profiles from NIR (black), MIR (blue) and TIRVIM (red). The orbits 2266 (Ls=182.8°,
 311 87°N, 37.4°E and local time of 7:55) and 2566 (Ls=197.1°, 50.9°N, -44.16°E and local time of
 312 17:24) were completed before the global dust storm and during the storm, respectively. The
 313 retrieved covariance matrix gives the error bars (one-sigma).

314

315 **3. Results**

316 **3.1 Seasonal trend of CO vertical distribution**

317 According to photochemical models, carbon monoxide is expected to be well-mixed from
 318 the surface up to ~50 km in mid-and low latitudes (Lefèvre and Krasnopolsky, 2017; Daerden et
 319 al., 2019). To verify these theoretical predictions, we considered the evolution of CO measured at
 320 two characteristic altitudes, 20 km and 40 km for two Martian years, 34 and 35, as a function of

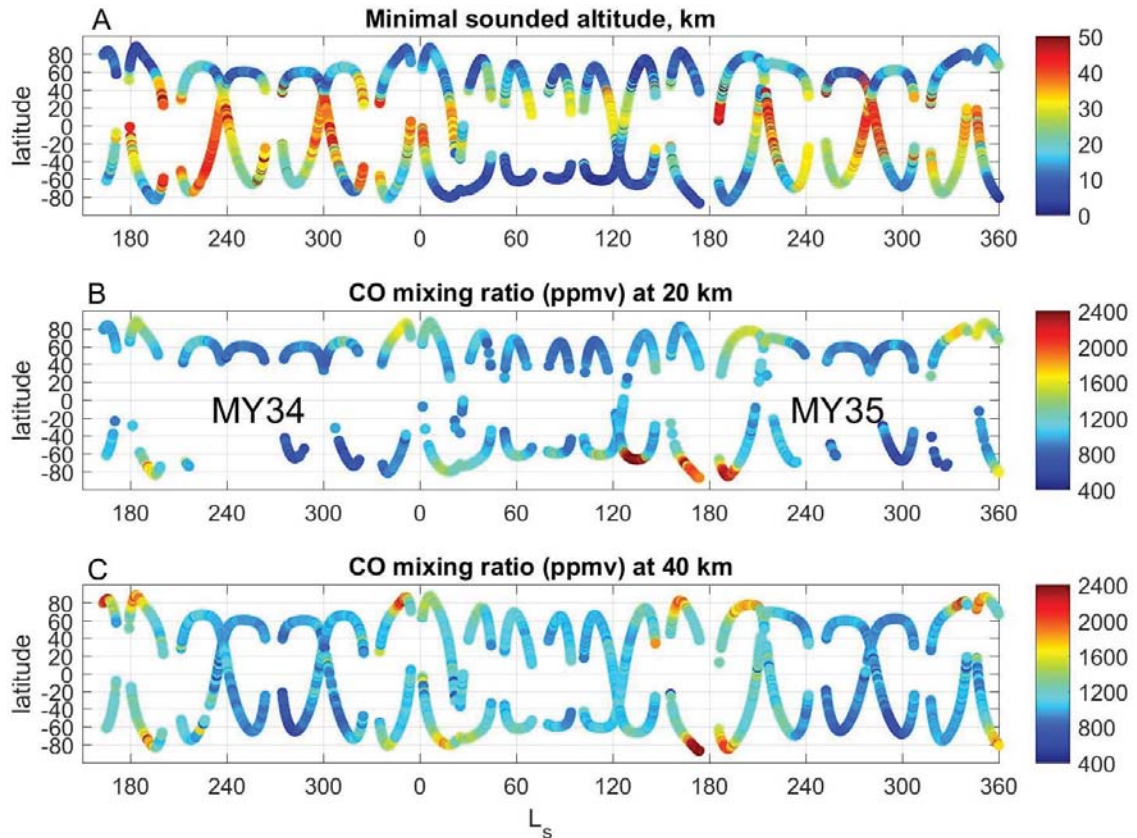
321 season and latitude (Figure 6). Below 20 km, profiles are strongly attenuated by aerosol extinction.
322 Above 40 km, CO absorption is getting fainter, increasing uncertainty with altitude. However,
323 aerosols frequently prevent accessing altitudes below 30 km (Figure 6A). Thus the measurements
324 at 20 km are only available in mid-to high-latitudes (30–80°) of both hemispheres. The
325 observations at two altitudes show an apparent difference in VMR and latitudinal variations. The
326 most considerable difference is observed toward the Poles, where downwelling from Hadley cell
327 circulation strongly impacts the shape of the CO VMR vertical profiles, as shown in Olsen et al.
328 (2021).

329 To follow the evolution of profiles with season and latitude in more detail, we grouped the
330 NIR and MIR data in 30° bins of Ls and presented it as a function of latitude and altitude for both
331 Martian years (Figure 7). Near the solstice in both hemispheres (Ls=60–120° and 240–300°), the
332 latitude coverage is limited to $\pm 60^\circ$. In the equinox period (Ls=330–30° and 150–210°), polar
333 latitudes are well covered. Whereas NIR can only measure CO below 50 km, the MIR channel can
334 probe CO up to 90 km in the most favorable cases, a higher altitude range than is accessible for
335 NIR.

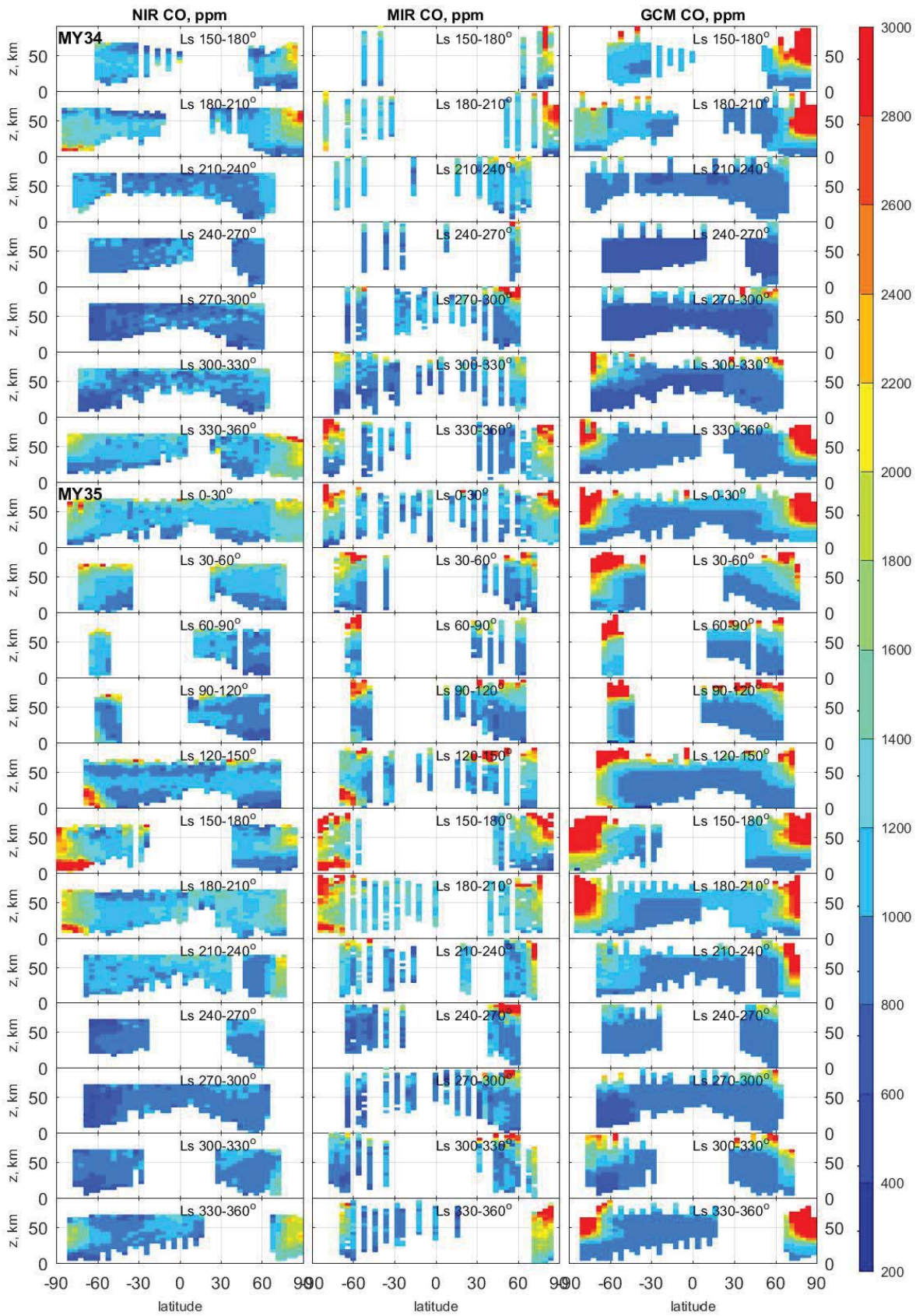
336 Overall, the vertical profiles of the CO mixing ratio were found far from being uniform.
337 The minimal values of CO were observed during the southern summer in middle-high southern
338 latitudes. This is consistent with trends observed by CRISM, while the NIR minimal values were
339 within 400–500 ppmv compared to 300–400 ppmv reported by CRISM ([Smith et al., 2018](#)). The
340 most prominent feature of the observed profiles is the pronounced maxima of CO VMR at high
341 latitudes. They are present in the lower atmosphere during southern winter and spring and above
342 40 km. These polar and mid-latitude enrichments are discussed further in subsections 3.3 and 3.5.

343 We have also calculated the seasonal distribution of CO with the LMD GCM and its
344 coupled photochemical module in the latest configuration described in Lefèvre et al. (2021). In
345 this dedicated simulation, the GCM is initialized at $L_s = 180^\circ$ of Martian year 33. At this date, CO
346 is set to a uniform (both in altitude and horizontal) initial mixing ratio of 1000 ppmv as previously

347 measured at low latitudes by CRISM (Smith et al., 2018) and MIR (Olsen et al., 2021). After a
 348 half Martian year of spin-up time, the model runs continuously until the end of Martian year 35
 349 while being constrained by the observed dust climatology (Montabone et al., 2020). The CO
 350 vertical distribution calculated by the LMD GCM (Figure 7c) is in good general agreement with
 351 NIR and MIR at low-to-mid latitudes. A seasonal minimum is evident in the perihelion season of
 352 both years considered here. However, the model largely overestimates the downwelling of
 353 thermospheric CO measured during the equinoctial periods at high latitudes. In contrast, near the
 354 surface, the strong enrichment of CO measured at high southern latitudes in late winter is absent
 355 in the GCM after $L_s = 150^\circ$.



356
 357 Figure 6. Carbon monoxide mixing ratios (ppmv) from ACS NIR occultations at two altitudes. A)
 358 The minimal sounded altitude in km, corresponding to aerosol attenuation of 0.07–0.08; B) CO
 359 VMR at 20 km; C) CO VMR at 40 km.



361 Figure 7. Seasonal distribution of CO mixing ratio observed by ACS NIR (left), ACS MIR
362 (middle) and LMD GCM (right): from MY34 on the top to MY35 on the bottom. Colorbar presents
363 the CO VMR in ppmv.

364 **3.2 The average CO mixing ratio**

365 The global average CO mixing ratio was the focus of many previous observations and 1D
366 modeling studies. To estimate the column-averaged mixing ratio of CO from the ACS profiles, we
367 integrated them from the bottom to below 35 km, where all three spectrometers have good
368 accuracy. We excluded the polar region and high latitudes where the CO₂ condensation-
369 sublimation cycle and the Hadley circulation make CO vertical distribution non-uniform (e.g.,
370 Figure 7). Thus, we limited ACS measurements to the middle-low latitudes (45°S–45°N). Figure
371 8 shows the seasonal evolution of column average CO values for NIR, MIR and TIRVIM
372 measurements, including the earlier results obtained from MIR (Olsen et al., 2021). The column
373 average values for MIR from Olsen et al. (2021) were integrated below 40 km. The CO mean value
374 shows a repeatable seasonal cycle from MY34 to MY35 with two maxima, the first and most
375 prominent at $L_s \sim 180^\circ$ and the second shortly after the spring equinox ($L_s = 0^\circ$) in the Northern
376 hemisphere.

377 By averaging the Figure 8 data along L_s , we obtain estimates of the annual mean mixing
378 ratio of CO: 971 ± 126 ppmv from NIR, 976 ± 142 ppmv from MIR. In case of TIRVIM the annual
379 average equals 812 ± 111 ppmv. The TIRVIM dataset resulted in the lowest average CO VMR,
380 possibly explained by its limited L_s coverage ($L_s = 240^\circ$ MY 34 to $L_s = 115^\circ$ MY 35). TIRVIM did
381 not probe the two equinox maxima near $L_s = 180^\circ$, resulting in underestimating the annual mean
382 VMR by at least 10%. Therefore, the three channels of ACS appear to produce altogether a fairly
383 reliable annual mean for CO of about 960 ppmv.

384 Figure 8 also shows the averages of CO measured in nadir by PFS/Mars Express in the 4.7
385 μm band (Bouche et al., 2021). A selection of PFS data for the same $\pm 45^\circ$ latitude belt was

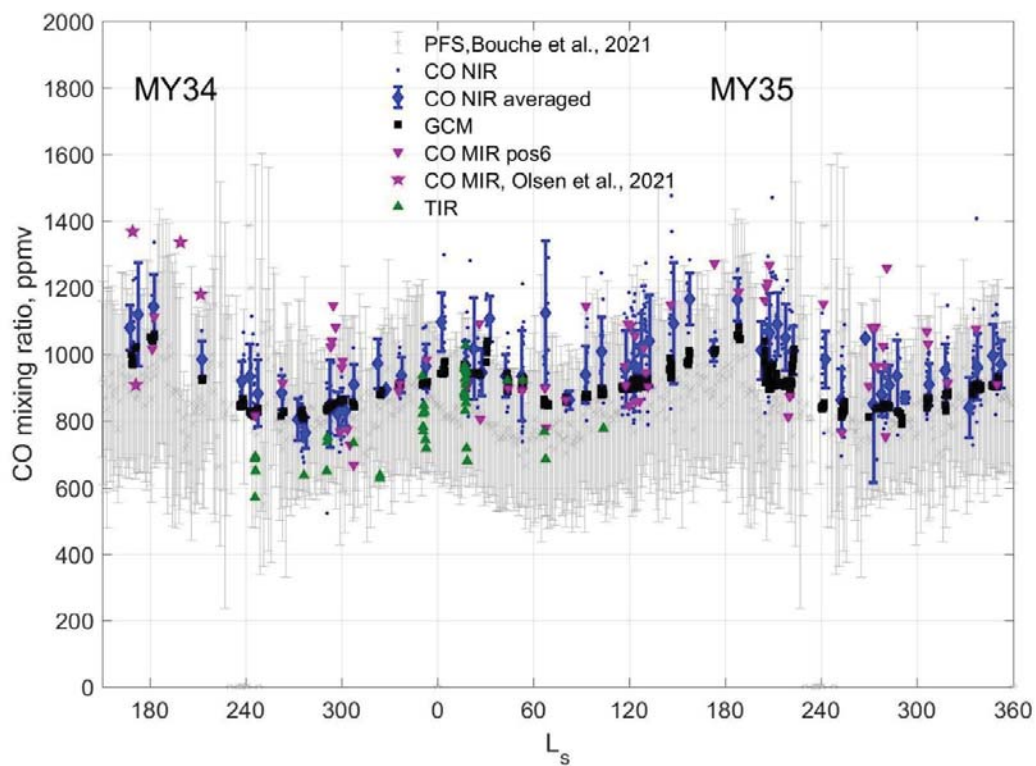
386 averaged within 1° bins of Ls for all available martian years (MY26–33). The seasonal trend agrees
387 well with ACS data.

388 Bouche et al. (2021) calculated a global mean for CO of 820 ppmv. Restricted to the mid-
389 to-low latitudes, the PFS dataset results in a global mean of 844 ppmv, in agreement with TIRVIM
390 results and 15% lower than NIR and MIR values. Our averaged values are also lower than the
391 CRISM and NOMAD global means, both being of about 800 ppmv (Smith et al., 2018; Smith et
392 al., 2021). From ground-based high-resolution observations Krasnopolsky (2015, 2017) obtained
393 an annual mean of 681 ± 13 ppmv, agreeing with the *in situ* measurements by Curiosity yielding
394 580 ± 80 ppmv (Franz et al., 2015, Trainer et al., 2019).

395 The mean CO mixing ratio calculated by the LMD GCM in Figure 8 shows a very good
396 quantitative agreement with the observations and qualitatively for what concerns the seasonal
397 variation. For both Martian years, the calculated mixing ratio is maximum around Ls = 180° . This
398 is in line with the seasonal evolution of CO at low-to-mid latitudes as measured by nadir-viewing
399 satellites (e.g., Smith et al., 2021) and is, more generally, typical of the seasonal evolution of all
400 long-lived non-condensable species (e.g., Trainer et al., 2019). This similarity suggests that the
401 CO₂ condensation-sublimation cycle at polar latitudes is the main driver of the seasonal signal in
402 CO visible in Figure 8. Photochemistry should also play a role in this signal, especially in the CO
403 decrease observed in the perihelion season, when larger amounts of H₂O at all altitudes lead to
404 much increased OH production. The relative contributions of the CO₂ cycle and of photochemistry
405 will be studied in a dedicated paper. Also, beyond the scope of the present study is the long-
406 standing problem of the underestimation of CO by models (Lefèvre and Krasnopolsky, 2017),
407 which requires overly lengthy simulations in order to reach the long-term equilibrium value of CO
408 in the GCM. Therefore, this historical problem should not be considered as ‘solved’ from the sole
409 good agreement found in Figure 8.

410 Addressing the difference between our observed global mean of 970 ppmv and the nadir
411 results from CRISM and NOMAD, ~ 800 ppmv, we can consider two possibilities: 1) their annual

412 average is a real global average, i.e., including the polar regions in summer where CO is low. The
 413 Figure 11 of Smith et al. (2018) shows the annual mean at low latitudes significantly larger than
 414 800 ppmv. Still, NOMAD CO in Smith et al. (2021) looks low. 2) The MIR/NIR vmr average is
 415 not exactly a column-average vmr because we don't see near surface mixing ratio in lower
 416 latitudes. If CO increases with altitude below 35 km, the vmr average will be larger than the
 417 column-average vmr. This effect should be verified, but we note that except for the polar latitudes
 418 in summer (the CO₂ sublimation) the CO vmr in the GCM never decreases close to the surface.



419
 420 Figure 8. The averaged values of CO from ACS profiles measured within $\pm 45^\circ$ latitude range and
 421 below 35 km. Blue points, purple and green triangles are individual NIR, MIR and TIRVIM
 422 occultations, respectively. Purple stars are the results of Olsen et al., 2021 from MIR position 7
 423 (integrated below 40 km). Blue diamonds with error bars are averages of NIR data binned within
 424 5° of L_s . Black squares are GCM model results corresponding to the NIR averages. Grey crosses
 425 are averages of PFS data (see text). All error bars are standard deviations.

426 3.3 Southern winter-spring CO enhancement

427 In the lower atmosphere, the maximal values of CO have been observed during the
428 Southern winter/beginning of spring in southern polar latitudes from $L_s=120^\circ$ to 200° . In MY 34
429 the observations began only at $L_s=163^\circ$ and the increase in mixing ratio below 20 km was detected
430 at $L_s=187^\circ$ – 195° when the occultations reached high southern latitudes (see Figure 7). In MY35
431 the coverage was better. The near-surface layer with enhanced CO has been observed from
432 $L_s=120^\circ$ to 195° by both NIR and MIR instruments (Figures 6, 7). Figure 9 shows individual CO
433 profiles obtained in southern high latitudes at $L_s=161^\circ$ – 174° and 185° – 195° . During the first
434 occultation campaigns in spring of 2018, a layer of CO at ~ 10 km reached values up to 3000–4000
435 ppmv. Twenty-five sols later ($L_s=185^\circ$) the layer moved to ~ 15 km with a maximum of 2500–
436 3000 ppmv and then disappeared at $L_s \geq 198^\circ$. Above this layer, the CO mixing ratio gradually
437 decreases to 2000 ppmv and then grows again at higher altitudes up to 3000 ppmv. The observed
438 CO maximum correlates with the temperature minimum observed below 30 km at high southern
439 latitudes. At $L_s=167^\circ$ – 174° the minimum is observed at 18–20 km with values as low as 125-135
440 K 10 km above the CO layer. At $L_s=185^\circ$ – 195° the minimum moved higher to 20-22 km with
441 warmer values about 140-150K.

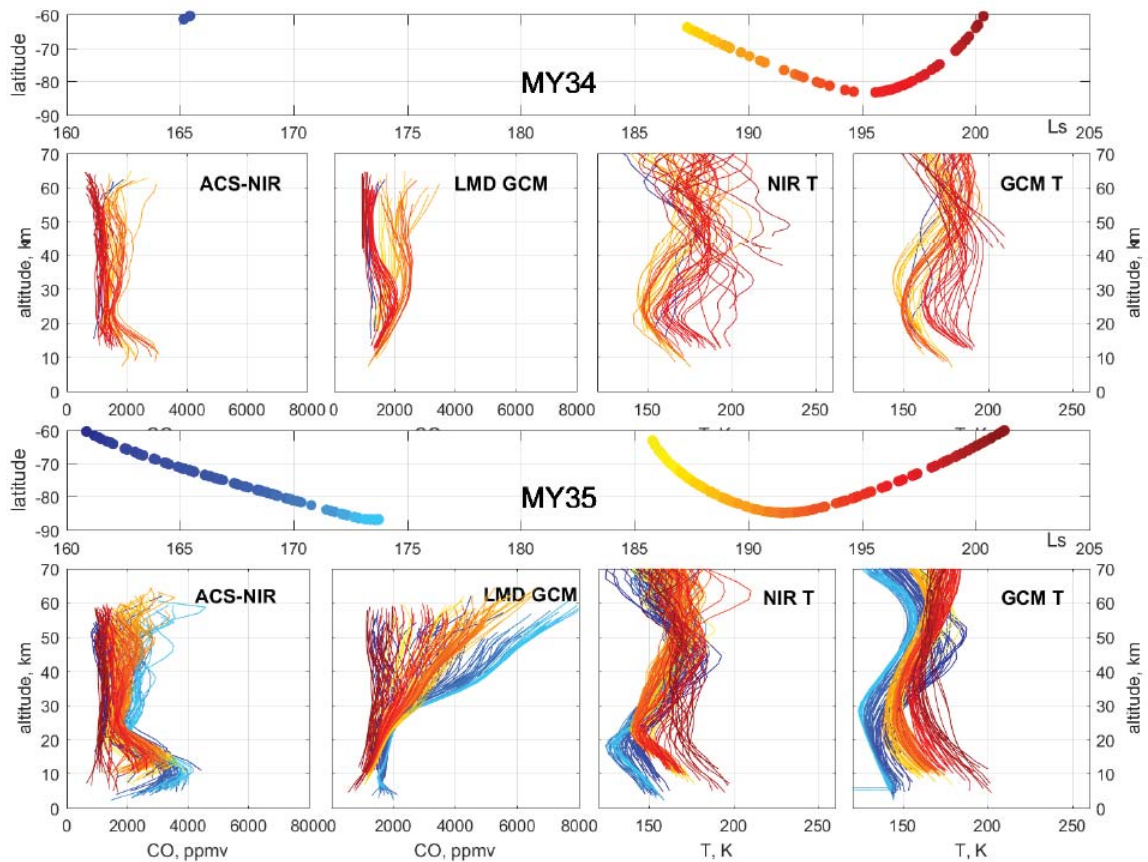
442 Enhancement of non-condensable species was previously observed in atmospheric argon
443 from measurements of the gamma ray spectrometer (GRS) operated on the Mars-Odyssey orbiter
444 ([Sprague et al., 2004](#), [2007](#)). The strong (a factor of 6) enhancement of Ar was measured over
445 south polar latitudes (75°S to 90°S) for two consecutive Mars years near the onset of southern
446 winter close to $L_s=90^\circ$. In winter over the northern polar regions there was no similar strong
447 enhancement of Ar and the seasonal peak was less obvious than in the south.

448 The nadir measurements of CO showed the strongest CO values at $L_s=140^\circ$ - 180° in the
449 southern hemisphere between 45° and 20°S with mixing ratio about 1100 ppmv (Smith et al., 2018;
450 Smith et al., 2021; Bouche et al., 2021). In nadir, the signal is dominated by absorption from the
451 denser layers and thus by the first scale heights below 20-30 km. Polar night regions are not

452 available due to limitation of data retrieval to solar zenith angles (SZA) $<80^\circ$. This could explain
453 why nadir experiments like CRISM and NOMAD do not show these maximal values at the poles
454 (Smith et al., 2021).

455 Unlike nadir, solar occultations can access higher latitudes during the equinox and polar
456 night seasons ($>60^\circ\text{S}$). At $L_s=60^\circ-150^\circ$ of MY35 ACS sounded at the edge of the southern polar
457 night approaching to $65-70^\circ\text{S}$. During the same period, CRISM was limited to 45°S . CO mixing
458 ratio apparently increased below 20 km at 60°S from 900 to 1500 ppmv during the $L_s=90^\circ-120^\circ$
459 interval. Closer to equinox, occultations moved to higher latitudes where the low-atmospheric
460 layer enriched progressively to 3000 ppmv at $L_s=120^\circ-150^\circ$ (see Figures 7, 8 and the SM) and
461 then 4000 ppmv at $L_s=170^\circ-175^\circ$ (Figures 8, 9 and the SM).

462 In the middle of the southern winter, the column-averaged CO mixing ratio calculated by
463 the LMD GCM reaches more than 4000 ppmv south of 75°S (not shown). However, the region
464 most enriched in CO in the model is located far in the polar night, and only the northernmost tip
465 of the CO-enriched layer near the surface is visible between $L_s = 120-150^\circ$ in Figure 7 (see also
466 the SM). In that layer, the modeled enrichment in CO appears to be underpredicted compared to
467 ACS, both in terms of absolute value and vertical extent. Later on, around the equinox, the GCM
468 no longer predicts an enriched layer of CO at high southern latitudes, in strong disagreement with
469 ACS which shows the persistence of an enriched layer in the $L_s = 180-210^\circ$ period. This indicates
470 that the breakup of the polar vortex enriched in CO (and in other non-condensable species) and the
471 subsequent mixing with midlatitude air occur too early with the settings of the LMD GCM used
472 here.



474

475 Figure 9. The evolution of the CO mixing ratio profiles for a sequence of occultations in the
 476 latitude range 60°S-90°S for martian years 34 and 35. (top) the latitude coverage; (left) ACS NIR
 477 measurements ; (right) LMD GCM simulation. Colours indicate Ls.

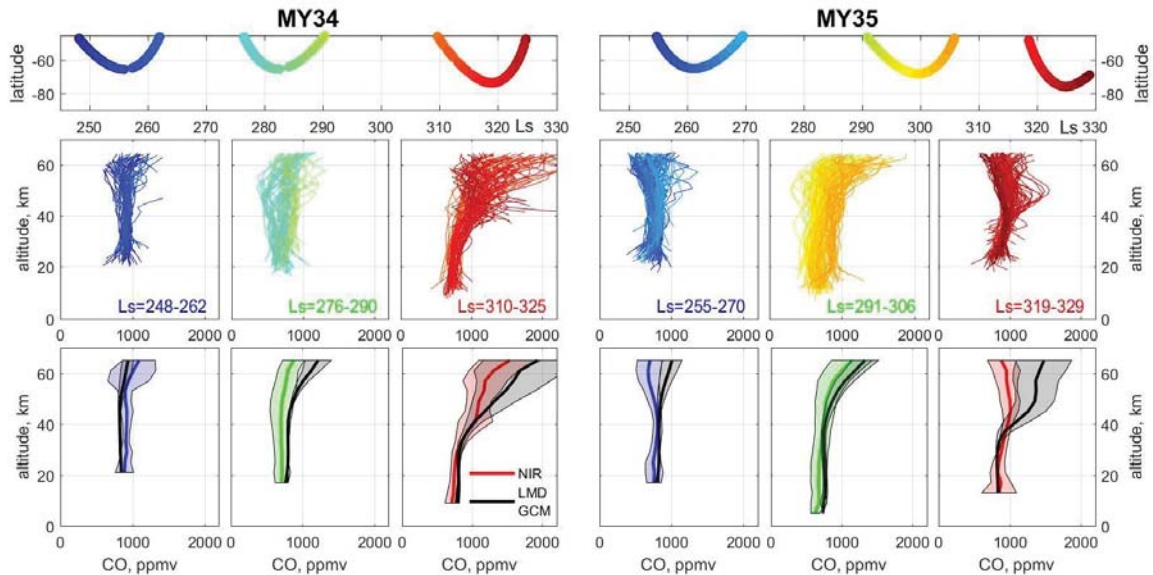
478

479 3.4. Southern summer CO depletion

480 CRISM observations, followed later by PFS and NOMAD nadir measurements, observed
 481 a minimum of CO abundance during the southern summer. This depletion was related to the
 482 sublimation of the southern CO₂ polar cap and resulted in the strong decrease of the CO column
 483 mixing ratio to the 300-500 ppmv from Ls=210° to Ls=330° in the high and middle southern
 484 latitudes (Smith et al., 2018, 2021).

485 In Figure 6b at 20 km, the CO depletion is seen in both MY 34 and 35 between Ls 250°
 486 and 330° in the southern hemisphere. During this period, Mars' GCM predicts a non-uniform

487 vertical distribution with strong vertical gradient and depletion near the surface (Holmes et al.,
 488 2019). So we decided to investigate the CO vertical distribution for the both observed southern
 489 summer seasons in more detail.



490
 491 Figure 10. The evolution of the CO mixing ratio profiles for a sequence of occultations in the
 492 latitude range 45°S–90°S and Ls from 245° to 330° for MY 34 and 35; (top) the latitude coverage;
 493 (middle) ACS NIR individual profiles for Ls bins; (bottom) the averaged profile for each Ls bin
 494 for ACS NIR and GCM LMD. The shaded area is the standard deviation.

495
 496 Figure 10 presents the evolution of the CO profiles in the latitude range from 45°S to 90°S
 497 and in the period from Ls=245 to 330° for both Martian years (34 and 35). In this dusty season,
 498 solar occultation can not sound deep in the atmosphere and the lowest altitude sounded is typically
 499 20 km above the surface except for Ls=310°–325° of MY34 and Ls=291°–306° in MY35 where
 500 we could probe down to 10 km. For both years we do not see a prominent gradient below 40 km
 501 except at Ls=309–325° of MY 34 where nearly-constant mixing ratios were observed below 35
 502 km, with an increase above. The average CO mixing ratio below 40 km was found to be 700–750
 503 ppmv which is higher than those obtained by CRISM between 50°S and 70°S (400 ppmv at
 504 Ls=260° and 700 ppmv at Ls=330°) and by PFS in the same period (~600 ppmv).

505 The CO profiles calculated in summer by the LMD GCM are in broad agreement with
506 ACS, but tend to anticipate the downwelling of enhanced CO mixing ratios by the Hadley
507 circulation at the approach of the equinox ($L_s = 318\text{--}330^\circ$ in Figure 10).

508

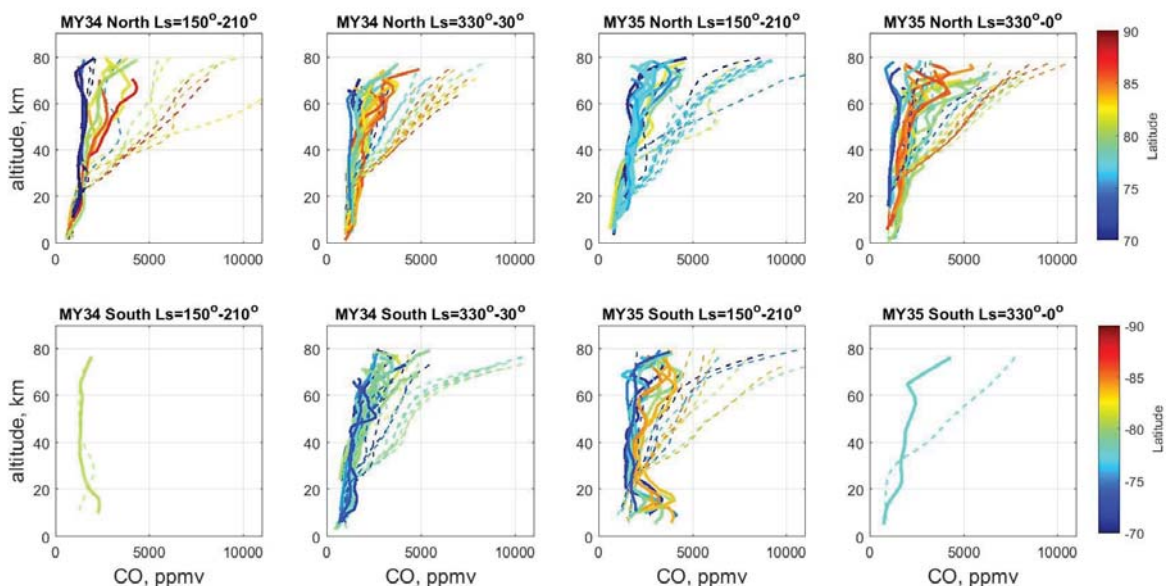
509 ***3.5 High altitude equinox and solstice enhancement***

510 The enhancement of CO at 50 km was first observed by Krasnopolsky (2014) based on CO
511 (2-1) dayglow observations at $4.7\ \mu\text{m}$ in the middle of northern summer ($L_s=110^\circ$) using the
512 CSHELL spectrograph at NASA IRTF. This dayglow is formed by CO molecules at 50 km. The
513 mixing ratio was found to increase from 1100 ppm at 40°S to 1600 ppm at 70°N . This behavior
514 was different from the trend observed at low altitudes, and was therefore attributed to the Hadley
515 circulation characterized by the equator-to-pole Hadley cells in equinox and pole-to-pole cell in
516 solstices. This circulation transports CO to the polar region where a downward flux of CO-rich air
517 occurs.

518 The NIR and MIR observations in the same period also support the increase of the CO
519 mixing ratio in the polar region above 50 km but the mixing ratio is much smaller than in the model
520 (Figure 7). The most sensitive for the study is the MIR spectrometer that can measure CO up to 80
521 km and has better accuracy compared to NIR at altitudes between 50 and 60 km (see section 2 and
522 SM). Figure 11 presents the observed and modelled mixing ratio profiles of CO in both
523 hemispheres at latitudes from 70° to 90° over a time period that encompasses equinox. The
524 equinoctial circulation is characterized by two symmetric Hadley cells facing each other about the
525 equator and carrying airmasses from the equator to the poles. The equinox periods covered concern
526 $L_s=150^\circ$ to 210° (MY35) for the northern spring and $L_s=330^\circ\text{--}30^\circ$ (MY 34/35) for the southern
527 spring. Before and after these ranges, the maxima are also observed, but the circulation is already
528 being rearranged.

529 At both equinoxes, the model is in rather good agreement with ACS at latitudes about 70° ,
530 but overestimates CO when moving to the poles. In the northern spring of MY34 and 35 the

531 observed profiles have shown a weak gradient from 1000 ppm at 10 km to 2000–3000 ppm at 60
 532 km depending on latitude with smaller values at lower latitudes. Above 60 km and at latitudes
 533 higher than 80°N the sharp increase of CO is visible at high latitudes to 5000 ppm at 80 km. The
 534 GCM profiles begin to grow from 30 km and overestimate the observations at least in 2 times since
 535 this altitude with 8000–10000 ppmv at 70–80 km. The same situation is observed in the southern
 536 spring except near the surface CO layer discussed in Section 3.3. In the southern and northern
 537 autumn of MY34 and 35, respectively, the CO mixing ratio changes from 1000 ppmv at 10 km to
 538 4000 ppmv at 70 km but with a sharper gradient compared to the spring. The model begins to
 539 overestimate the data in some cases from 20 km. This suggests that the intensity of the Hadley
 540 cells at the equinox is too strong in the GCM, bringing too much CO from its region of production
 541 in the high atmosphere.



542
 543 Figure 11. The evolution of the CO mixing ratio profiles for sequence of occultations for equinox
 544 season ($L_s=150^\circ-210^\circ$ and $330^\circ-30^\circ$) for MY 34 and 35 in high southern and northern latitudes
 545 (-70° to -90° and 70° to 90° , respectively). Colors indicate the latitude variations. Solid curves
 546 are the ACS MIR data, dashed curves represent the LMD GCM simulation.

547

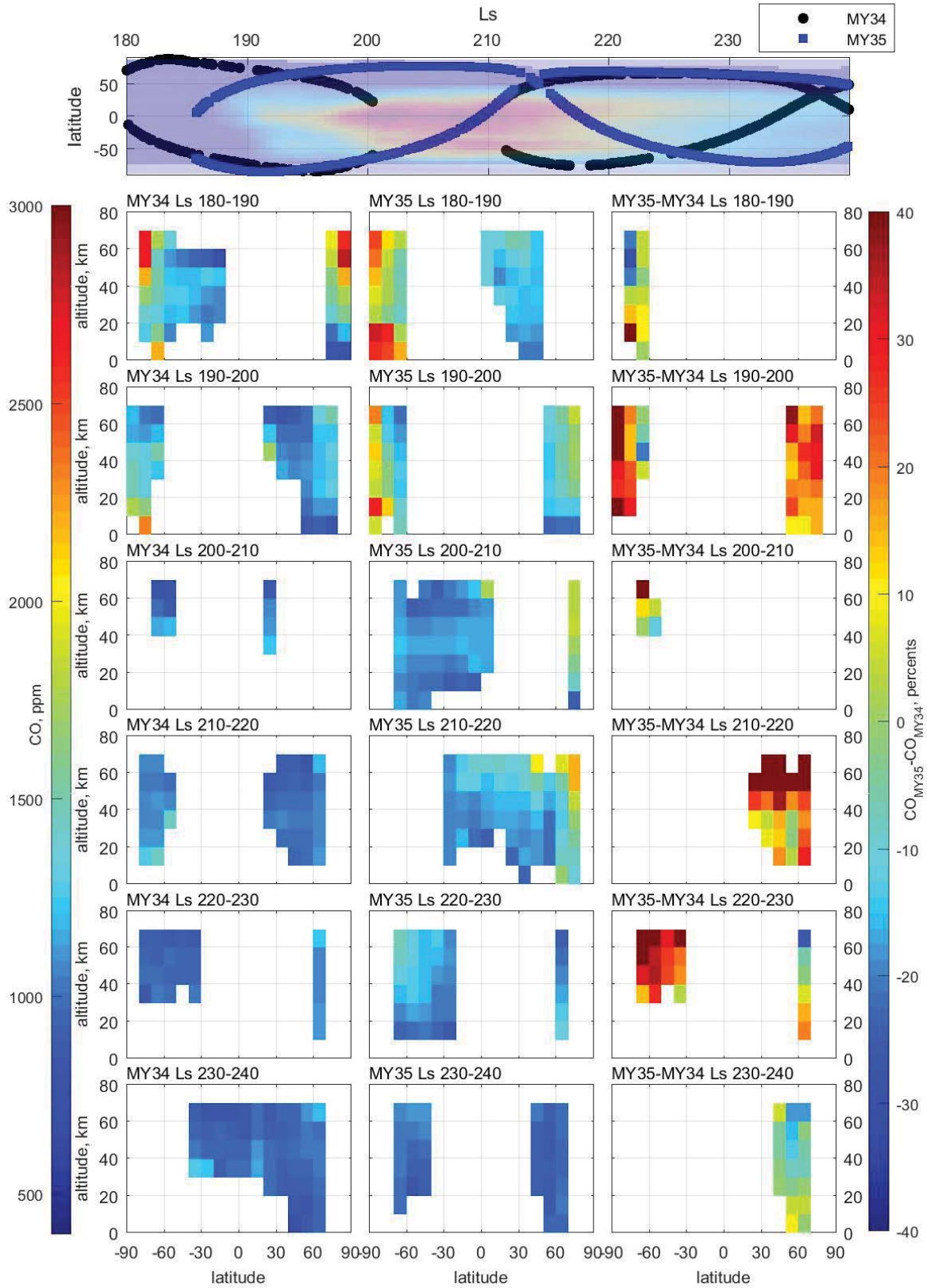
548 **3.6 Interannual variability due to the GDS of MY 34**

549 In the lower atmosphere, provided there is water vapor, the loss of CO by reaction with
550 OH exceeds its production. It should then end up making CO sensitive to changes in water content.
551 Nevertheless, the lifetime of about five terrestrial years does not authorize prominent chemical
552 variations of CO at the seasonal timescales.

553 MY 34 was characterized by the GDS that began at approximately $L_s=185^\circ$ (Guzewith et
554 al., 2019; Smith, 2019) in the Northern hemisphere. The first phase of the storm from $L_s=185^\circ$ to
555 192° is better defined as a regional dust storm which then turned into a massive global event at
556 $L_s=197^\circ$ after the secondary massive dust injection over Tharsis (Montabone et al., 2020). The
557 decay phase of the storm started at $L_s=210^\circ$ and lasted until $L_s=240^\circ$. It is now known that GDSs
558 profoundly impact water vertical distribution in the atmosphere by transferring H_2O to high
559 altitudes (Fedorova et al., 2018; 2020, 2021; Heavens et al., 2018; Aoki et al., 2019). Dust heats
560 the atmosphere and amplifies the Hadley cell circulation which in turn increases the altitude of the
561 hygropause. The water vertical distribution during the GDS of MY 34 was studied with ACS and
562 NOMAD on TGO (Fedorova et al., 2020; Aoki et al., 2019; Belyaev et al., 2021) and SPICAM
563 (SPectroscopy for the Investigation of the Characteristics of the. Atmosphere of Mars) on Mars
564 Express using the solar occultation technique (Fedorova et al., 2021). Water was observed up to
565 120 km with mixing ratios of 20–50 ppmv. More water in the middle atmosphere provides more
566 OH (hydroxyl) radicals once H_2O is photolyzed. This has the effect of boosting the rate of reactions
567 between CO and OH, and hence the reformation of CO_2 . So, the sensitivity of CO to water activity
568 can provide an insight into the stability of the Martian atmosphere.

569 The first ever profiles of CO were produced by ACS MIR and reported for the period from
570 $L_s=163^\circ$ (pre-storm) to $L_s=220^\circ$ (decay phase), which showed how CO was affected by this event
571 (Olsen et al., 2021). After the onset of the dust storm, the mean CO mixing ratio was observed to
572 decrease from 1260 to 1070 ppmv below 40 km which was explained as the enhanced presence of
573 H_2O and thus OH that subsequently accelerated CO loss. The same occurred at high altitudes
574 where the rise of hygropause also resulted in the decrease of CO.

575 With two Martian years of observations, we can compare the CO vertical profiles during
576 the GDS period of MY 34 with the more regular MY 35 using ACS NIR data. The panels of Figure
577 7 at $L_s=180^\circ-210^\circ$ clearly show more CO in the high southern latitudes during MY 35 than during
578 MY 34. On the other hand, CO in high northern latitudes at altitudes above 40 km is more abundant
579 in MY 34. Over $L_s=210^\circ-240^\circ$, the observed CO mixing ratios between 30 and 60 km in low
580 latitudes ($30^\circ\text{S}-30^\circ\text{N}$) is higher in MY 35 compared to MY 34. As shown in Figure 1, solar
581 occultations in different years can have different latitudinal distribution and the observations can
582 relate to different L_s . To exclude these uncertainties, we have selected smaller latitude bins than
583 in Figure 7 (10° of L_s versus 30° of L_s) to compare nearly close in L_s and latitude observations for
584 two years (Figure 12). We average the ACS dataset inside 10° of L_s , 10° of latitude and 10 km of
585 altitude. In Figure 12 the CO values for the selected bins are shown as altitude-latitude maps for
586 MY34 and MY35 together with their relative difference, where the L_s -latitude coverage permits.
587
588



590 Figure 12. The latitudinal trend of the CO mixing ratio vertical profiles in ppmv into 10° Ls bins
591 from Ls=180° to 240° for MY34 (left) and MY35 (middle) and their relative difference in percent
592 (right). On the top panel is the seasonal distribution of ACS NIR solar occultation observations for
593 MY 34 and 35 at Ls=180–240°. The colored background is the dust optical depth distribution in 9
594 μm for MY 34 from Montabone et al. (2020) with red color corresponding to maximal optical
595 depth and blue color corresponding to minimal.

596

597 For the first Ls bin (180°–190°) the data from the two years overlap only in high southern
598 latitudes just before the beginning of GDS and the difference near 60°S does not exceed 10%.
599 From Ls=190° to 230°, during the maximal dust loading, the CO mixing ratio in MY35 is larger
600 than in MY34 at 30–40% both in the northern and southern hemispheres. On the decay of GDS, at
601 Ls=230°–240°, the observations overlap in middle northern latitudes, and the difference between
602 two years was within 10% again. The decrease of the CO mixing ratio in MY34 during the GDS
603 is anti-correlated with increase of water vapor abundance in the atmosphere in both hemispheres
604 for the same period (see Figure 8 of the SM). The notable CO depletion during the GDS of MY34
605 can indicate the response of CO₂ production rate to the strong increase in water vapor during this
606 period (see., e.g. Fedorova et al., 2020).

607

608 **Conclusions**

609 We analyzed a large dataset of CO vertical profiles made using solar occultation
610 observations of the three ACS spectrometers onboard the ExoMars Trace Gas Orbiter. The data
611 has been collected from April 2018 (Ls=163° of MY 34) to March 2021 (Ls=360° of MY 35) and
612 covers 1.5 Martian years. The most dense dataset is coming from the ACS NIR spectrometer
613 collected for this period more than 6200 occultations. Based on this dataset we made the
614 simultaneous retrieval of the CO₂ density and temperature profiles and CO mixing ratio in the
615 spectral range of 1.65-1.67 μm (order 49 of the spectrometer) including of the 1.65 μm CO₂ band

616 and the CO (3-0) overtone at 1.67 μm in range of altitude from 0 to 60 km for CO. The ACS
617 TIRVIM provides the second dense dataset about 1000 occultations but the observations stopped
618 in December 2019. The CO mixing ratio was retrieved based on the strong 4.7 μm CO absorption
619 band and the CO₂ density from 4.9 μm band. The low SNR and spectral resolution limit the
620 sounding altitude to 50 km. ACS MIR, the most sensitive channel of ACS has performed 620
621 occultations up to the end of MY35 and provided the measurements of CO VMR vertical profiles
622 in 2.3 μm absorption band based on CO₂ density and temperature retrieved from simultaneous
623 measurements of ACS NIR in the range of altitude from 0 to 80 km.

624 With this dataset we presented the first detailed analysis of CO vertical distribution on the
625 long timescale and studied seasonal and latitudinal variation during the martian year :

- 626 1) We found a mean CO VMR of ~ 960 ppmv in the range of 10-35 km and in the low and
627 middle latitudes (from 45°S to 45°N). Our averaged values are lower than the CRISM,
628 NOMAD and PFS/MEX global means from nadir measurements, both being of about 800
629 ppmv (Smith et al., 2018; Smith et al., 2021; Bouche et al., 2021). The CO mean value
630 shows a repeatable seasonal cycle from MY34 to MY35 with two maxima, the first and
631 largest of the two at $L_s \sim 180^\circ$ and the second shortly after spring equinox ($L_s = 0^\circ$) in the
632 Northern hemisphere.
- 633 2) We found a strong enrichment of CO near the surface during the southern winter and spring
634 ($L_s = 100-200^\circ$) in middle and high southern latitudes with a layer of 3000-4000 ppm at 10-
635 20 km corresponding to local depletion of CO₂. In the Northern polar winter atmosphere,
636 such a layer of CO was not observed. The GCM does not predict the enrichment in CO in
637 this period, both in terms of absolute value and vertical extent. This indicates that the
638 breakup of the polar vortex enriched in CO (and in other non-condensable species) and the
639 subsequent mixing with midlatitude air occur too early with the settings of the LMD GCM
640 used here.

- 641 3) In the equinox seasons both in the northern and southern spring, we found an increase of
642 CO mixing ratio above 50 km to 3000–4000 ppmv which is related to the downwelling
643 flux of the equinox Hadley circulation on Mars above the Poles enriched of CO molecules.
644 The comparison with the general circulation chemical model has shown that it tends to
645 overestimate the intensity of this process, bringing too much CO from its region of
646 production in the high atmosphere.
- 647 4) The minimum of CO observed in the southern summer in the high and middle southern
648 latitudes has average VMRs of 700–750 ppmv in the low atmosphere and agrees well with
649 nadir measurements by CRISM/MRO and PFS/MEX even they have lower values of 400-
650 700 ppmv and ~600 ppmv, respectively, in the same period. The CO profiles calculated in
651 southern summer by the LMD GCM are in broad agreement with ACS.
- 652 5) The observations during the two Martian years allow us to study the interannual variability
653 for the year with the global dust storm (MY34) and year without GDS (MY35). We
654 observed the depletion of the CO mixing ratio at 30-40% both in the northern and southern
655 hemispheres during the global dust storm of MY34 compared with the calm MY35. The
656 decrease of the CO mixing ratio in MY34 can indicate the response of CO₂ production rate
657 to the increase of water vapor abundance in the atmosphere for the same period that
658 suggests an impact of HO_x chemistry on the CO abundance.

659

660 **Acknowledgments**

661 The ExoMars mission is a joint mission of the European Space Agency (ESA) and
662 Roscosmos. The ACS experiment is led by the Space Research Institute (IKI) in Moscow, assisted
663 by LATMOS in France. The science operations of ACS are funded by Roscosmos and ESA.
664 Authors affiliated with IKI acknowledge funding from the Ministry of Science and High Education
665 of Russia. Authors affiliated with LATMOS acknowledge funding from CNES and Centre
666 National de la Recherche Scientifique (CNRS). Authors affiliated with the University of Oxford

667 acknowledge funding from the UK Space Agency under grants ST/T002069/1, ST/R001502/1 and
668 ST/P001572/1.

669 **Data availability.**

670 ACS data are available from ESA Planetary Science Archive (PSA) Level 2
671 <https://archives.esac.esa.int/psa/#!Table%20View/ACS=instrument>. The CO vertical profiles
672 generated from ACS measurements and analyzed in this study are available on
673 ftp://193.232.13.174/ACS_NIR_Results/CO_climatology/ for review purposes. Data will be
674 stored in Mendeley repository at Fedorova, Anna (2022), “Carbon monoxide (CO) on Mars from
675 ACS occultations (MY34-35)”, Mendeley Data, V1, doi: 10.17632/w2b89yr6x5.1.

676

677

678 **Reference**

679

680 Alday, J., Trokhimovskiy, A., Irwin, P. G. J., Wilson, C. F., Montmessin, F., Lefèvre, F., et al. (2021).

681 Isotopic fractionation of water and its photolytic products in the atmosphere of Mars. *Nature*

682 *Astronomy*, 5(9), 943–950. <https://doi.org/10.1038/s41550-021-01389-x>

683 Alday, J., Wilson, C. F., Irwin, P. G. J., Olsen, K. S., Baggio, L., Montmessin, F., et al. (2019). Oxygen

684 isotopic ratios in Martian water vapour observed by ACS MIR on board the ExoMars Trace Gas

685 Orbiter. *Astronomy & Astrophysics*, 630, A91. <https://doi.org/10.1051/0004-6361/201936234>

686 Aoki, S., Vandaele, A. C., Daerden, F., Villanueva, G. L., Liuzzi, G., Thomas, I. R., et al. (2019). Water

687 Vapor Vertical Profiles on Mars in Dust Storms Observed by TGO/NOMAD. *Journal of*

688 *Geophysical Research: Planets*, 124(12), 3482–3497. <https://doi.org/10.1029/2019je006109>

689 Belyaev, D. A., Fedorova, A. A., Trokhimovskiy, A., Alday, J., Montmessin, F., Korablev, O. I., et al.

690 (2021). Revealing a High Water Abundance in the Upper Mesosphere of Mars With ACS

691 Onboard TGO. *Geophysical Research Letters*, 48(10), e2021GL093411.

692 <https://doi.org/10.1029/2021GL093411>

693 Billebaud, F., Brillet, J., Lellouch, E., Fouchet, T., Encrenaz, T., Cottini, V., et al. (2009). Observations of

694 CO in the atmosphere of Mars with PFS onboard Mars Express. *Planet. Space Sci.*, 57, 1446–

695 1457. <https://doi.org/10.1016/j.pss.2009.07.004>

696 Billebaud, F., Maillard, J. P., Lellouch, E., & Encrenaz, T. (1992). The spectrum of Mars in the (1-0)

697 vibrational band of CO. *Astronomy and Astrophysics*, 261, 647–657.

698 Billebaud, F., Rosenqvist, J., Lellouch, E., Maillard, J.-P., Encrenaz, T., & Hourdin, F. (1998).

699 Observations of CO in the atmosphere of Mars in the (2-0) vibrational band at 2.35 microns.

700 *Astronomy and Astrophysics*, 333, 1092–1099.

701 Bouche, J., Bauduin, S., Giuranna, M., Robert, S., Aoki, S., Vandaele, A. C., et al. (2019). Retrieval and

702 characterization of carbon monoxide (CO) vertical profiles in the Martian atmosphere from

703 observations of PFS/MEX. *Journal of Quantitative Spectroscopy and Radiative Transfer*, 238,

704 106498. <https://doi.org/10.1016/j.jqsrt.2019.05.009>

705 Bouche, J., Coheur, P.-F., Giuranna, M., Wolkenberg, P., Nardi, L., Amoroso, M., et al. (2021). Seasonal

706 and Spatial Variability of Carbon Monoxide (CO) in the Martian Atmosphere From PFS/MEX

707 Observations. *Journal of Geophysical Research: Planets*, 126(2), e2020JE006480.
708 <https://doi.org/10.1029/2020JE006480>

709 Clancy, R. T., Muhleman, D. O., & Berge, G. L. (1990). Global changes in the 0–70 km thermal structure
710 of the Mars atmosphere derived from 1975 to 1989 microwave CO spectra. *Journal of*
711 *Geophysical Research: Solid Earth*, 95(B9), 14543–14554.
712 <https://doi.org/10.1029/JB095iB09p14543>

713 Daerden, F., Neary, L., Viscardy, S., García Muñoz, A., Clancy, R. T., Smith, M. D., et al. (2019). Mars
714 atmospheric chemistry simulations with the GEM-Mars general circulation model. *Icarus*, 326,
715 197–224. <https://doi.org/10.1016/j.icarus.2019.02.030>

716 Encrenaz, T., Fouchet, T., Melchiorri, R., Drossart, P., Gondet, B., Langevin, Y., et al. (2006). Seasonal
717 variations of the martian CO over Hellas as observed by OMEGA/Mars Express. *Astron.*
718 *Astrophys.*, 459, 265–270. <https://doi.org/10.1051/0004-6361:20065586>

719 Fedorova, A. A., Montmessin, F., Korablev, O., Luginin, M., Trokhimovskiy, A., Belyaev, D. A., et al.
720 (2020). Stormy water on Mars: The distribution and saturation of atmospheric water during the
721 dusty season. *Science*, 367(6475), 297–300. <https://doi.org/10.1126/science.aay9522>

722 Fedorova, A., Bertaux, J. L., Betsis, D., Montmessin, F., Korablev, O., Maltagliati, L., & Clarke, J.
723 (2018). Water vapor in the middle atmosphere of Mars during the 2007 global dust storm. *Icarus*,
724 300, 440–457. <https://doi.org/10.1016/j.icarus.2017.09.025>

725 Fedorova, A., Montmessin, F., Korablev, O., Lefèvre, F., Trokhimovskiy, A., & Bertaux, J.-L. (2021).
726 Multi-Annual Monitoring of the Water Vapor Vertical Distribution on Mars by SPICAM on Mars
727 Express. *Journal of Geophysical Research: Planets*, 126(1), e2020JE006616.
728 <https://doi.org/10.1029/2020JE006616>

729 Forget, F., Hourdin, F., Fournier, R., Hourdin, C., Talagrand, O., Collins, M., et al. (1999). Improved
730 general circulation models of the Martian atmosphere from the surface to above 80 km. *J.*
731 *Geophys. Res.*, 104, 24155–24176. <https://doi.org/10.1029/1999JE001025>

732 Forget, F., Millour, E., Montabone, L., & Lefevre, F. (2008). Non Condensable Gas Enrichment and
733 Depletion in the Martian Polar Regions, 1447, 9106. Presented at the Third International
734 Workshop on The Mars Atmosphere: Modeling and Observations.

735 Franz, H. B., Trainer, M. G., Wong, M. H., Mahaffy, P. R., Atreya, S. K., Manning, H. L. K., & Stern, J.

736 C. (2015). Reevaluated martian atmospheric mixing ratios from the mass spectrometer on the
737 Curiosity rover. *Planetary and Space Science*, 109–110, 154–158.
738 <https://doi.org/10.1016/j.pss.2015.02.014>

739 Gordon, I. E., Rothman, L. S., Hill, C., Kochanov, R. V., Tan, Y., Bernath, P. F., et al. (2017). The
740 HITRAN2016 molecular spectroscopic database. *J. Quant. Spectrosc. Radiat. Transfer*, 203, 3–
741 69. <https://doi.org/10.1016/j.jqsrt.2017.06.038>

742 Guzewich, S. D., Lemmon, M., Smith, C. L., Martínez, G., Vicente-Retortillo, Á. de, Newman, C. E., et
743 al. (2019). Mars Science Laboratory Observations of the 2018/Mars Year 34 Global Dust Storm.
744 *Geophysical Research Letters*, 46(1), 71–79. <https://doi.org/10.1029/2018GL080839>

745 Heavens, N. G., Kleinböhl, A., Chaffin, M. S., Halekas, J. S., Kass, D. M., Hayne, P. O., et al. (2018).
746 Hydrogen escape from Mars enhanced by deep convection in dust storms. *Nature Astronomy*,
747 2(2), 126–132. <https://doi.org/10.1038/s41550-017-0353-4>

748 Holmes, J. A., Lewis, S. R., Patel, M. R., & Smith, M. D. (2019). Global analysis and forecasts of carbon
749 monoxide on Mars. *Icarus*, 328, 232–245. <https://doi.org/10.1016/j.icarus.2019.03.016>

750 Kaplan, L. D., Connes, J., & Connes, P. (1969). Carbon Monoxide in the Martian Atmosphere. *Astrophys.*
751 *J.*, 157, L187. <https://doi.org/10.1086/180416>

752 Korablev, O., Montmessin, F., Trokhimovskiy, A., Fedorova, A. A., Shakun, A. V., Grigoriev, A. V., et
753 al. (2018). The Atmospheric Chemistry Suite (ACS) of Three Spectrometers for the ExoMars
754 2016 Trace Gas Orbiter. *Space Science Reviews*, 214(1), 7. [https://doi.org/10.1007/s11214-017-](https://doi.org/10.1007/s11214-017-0437-6)
755 0437-6

756 Krasnopolsky, V. A. (2003). Spectroscopic mapping of Mars CO mixing ratio: Detection of north-south
757 asymmetry. *J. Geophys. Res.*, 108, 5010. <https://doi.org/10.1029/2002JE001926>

758 Krasnopolsky, V. A. (2007). Long-term spectroscopic observations of Mars using IRTF/CSHELL:
759 Mapping of O₂ dayglow, CO, and search for CH₄. *Icarus*, 190, 93–102.
760 <https://doi.org/10.1016/j.icarus.2007.02.014>

761 Krasnopolsky, V. A. (2014). Observations of the CO dayglow at 4.7μm on Mars: Variations of
762 temperature and CO mixing ratio at 50km. *Icarus*, 228, 189–196.
763 <https://doi.org/10.1016/j.icarus.2013.10.008>

764 Krasnopolsky, V. A. (2015). Variations of carbon monoxide in the martian lower atmosphere. *Icarus*,

765 253, 149–155. <https://doi.org/10.1016/j.icarus.2015.03.006>

766 Krasnopolsky, V. A. (2017). Annual mean mixing ratios of N₂, Ar, O₂, and CO in the martian
767 atmosphere. *Planetary and Space Science*, 144, 71–73. <https://doi.org/10.1016/j.pss.2017.05.009>

768 Lefèvre, F., & Krasnopolsky, V. (2017). Atmospheric Photochemistry. In R. M. Haberle, R. T. Clancy, F.
769 Forget, M. D. Smith, & R. W. Zurek (Eds.), *The Atmosphere and Climate of Mars* (pp. 405–432).
770 Cambridge University Press.

771 Lefèvre, F., Lebonnois, S., Montmessin, F., & Forget, F. (2004). Three-dimensional modeling of ozone
772 on Mars. *J. Geophys. Res.*, 109(E7), E07004. <https://doi.org/10.1029/2004JE002268>

773 Lellouch, E., Encrenaz, T., Phillips, T., Falgarone, E., & Billebaud, F. (1991). Submillimeter observations
774 of CO in Mars' atmosphere. *Planetary and Space Science*, 39(1), 209–212.
775 [https://doi.org/10.1016/0032-0633\(91\)90143-X](https://doi.org/10.1016/0032-0633(91)90143-X)

776 Li, G., Gordon, I.E., Rothman L.S., Tan, Y., Hu, S.-M., Kassi, S., Campargue, A. and Medvedev, E.S.
777 (2015). «ROVIBRATIONAL LINE LISTS FOR NINE ISOTOPOLOGUES OF THE CO
778 MOLECULE IN THE X 1 Σ + GROUND ELECTRONIC STATE». *The Astrophysical Journal
779 Supplement Series* 216 (1): 15. <https://doi.org/10.1088/0067-0049/216/1/15>.

780 McElroy, M. B. and Donahue, T.B. (1972). Stability of the Martian Atmosphere. *Science* 177 (4053): 986–
781 88. <https://doi.org/10.1126/science.177.4053.986>.

782 Millour E., Francois Forget, Aymeric Spiga, Margaux Vals, Vladimir Zakharov, Luca Montabone, Franck
783 Lefèvre, Franck Montmessin, Jean-Yves Chaufray, Miguel López-Valverde, Francisco González-
784 Galindo, Stephen Lewis, Peter Read, Marie-Christine Desjean, and Fabrice Cipriani The Mars
785 Climate Database (MCD version 5.3), Geophysical Research Abstracts, Vol. 21, EGU2019-7153,
786 2019, EGU General Assembly 2019

787 Montabone, L., Spiga, A., Kass, D. M., Kleinböhl, A., Forget, F., & Millour, E. (2020). Martian Year 34
788 Column Dust Climatology from Mars Climate Sounder Observations: Reconstructed Maps and
789 Model Simulations. *J. Geophys. Res.*

790 Nair, H., Allen, M., Anbar, A. D., Yung, Y. L., & Clancy, R. T. (1994). A Photochemical Model of the
791 Martian Atmosphere. *Icarus*, 111(1), 124–150. <https://doi.org/10.1006/icar.1994.1137>

792 Olsen, K. S., Lefèvre, F., Montmessin, F., Fedorova, A. A., Trokhimovskiy, A., Baggio, L., et al. (2021).
793 The vertical structure of CO in the Martian atmosphere from the ExoMars Trace Gas Orbiter.

794 *Nature Geoscience*, 14(2), 67–71. <https://doi.org/10.1038/s41561-020-00678-w>

795 Parkinson, T. D., and D. M. Hunten. (1972). Spectroscopy and Aeronomy of O₂ on Mars. *Journal of the*
796 *Atmospheric Sciences* 29 (7): 1380–90. [https://doi.org/10.1175/1520-](https://doi.org/10.1175/1520-0469(1972)029<1380:saaooo>2.0.co;2)
797 [0469\(1972\)029<1380:saaooo>2.0.co;2](https://doi.org/10.1175/1520-0469(1972)029<1380:saaooo>2.0.co;2).

798 Shakun, A., Ignatiev, N., Luginin, M., Grigoriev, A., Moshkin, B., Grassi, D., Arnold, G. (2018).
799 ACS/TIRVIM: Calibration and first results, Proc. SPIE 10765, Infrared Remote Sensing and
800 Instrumentation XXVI, 107650E, <https://doi.org/10.1117/12.2322163>.

801 Sindoni, G., Formisano, V., & Geminale, A. (2011). Observations of water vapour and carbon monoxide
802 in the Martian atmosphere with the SWC of PFS/MEX. *Planet. Space Sci.*, 59, 149–162.
803 <https://doi.org/10.1016/j.pss.2010.12.006>

804 Smith, M. D. (2019). THEMIS Observations of the 2018 Mars Global Dust Storm. *Journal of*
805 *Geophysical Research: Planets*, 124(11), 2929–2944. <https://doi.org/10.1029/2019je006107>

806 Smith, M. D., Daerden, F., Neary, L., & Khayat, A. S. J. (2018). The climatology of carbon monoxide
807 and water vapor on Mars as observed by CRISM and modeled by the GEM-Mars general
808 circulation model. *Icarus*, 301, 117–131. <https://doi.org/10.1016/j.icarus.2017.09.027>

809 Smith, M. D., Daerden, F., Neary, L., Khayat, A. S. J., Holmes, J. A., Patel, M. R., et al. (2021). The
810 climatology of carbon monoxide on Mars as observed by NOMAD nadir-geometry observations.
811 *Icarus*, 362, 114404. <https://doi.org/10.1016/j.icarus.2021.114404>

812 Smith, M. D., Wolff, M. J., Clancy, R. T., & Murchie, S. L. (2009). Compact Reconnaissance Imaging
813 Spectrometer observations of water vapor and carbon monoxide. *J. Geophys. Res.*, 114, E00D03.
814 <https://doi.org/10.1029/2008JE003288>

815 Sprague, A. L., Boynton, W. V., Forget, F., Lian, Y., Richardson, M., Starr, R., et al. (2012). Interannual
816 similarity and variation in seasonal circulation of Mars' atmospheric Ar as seen by the Gamma
817 Ray Spectrometer on Mars Odyssey. *Journal of Geophysical Research: Planets*, 117(E4).
818 <https://doi.org/10.1029/2011JE003873>

819 Sprague, A. L., Boynton, W. V., Kerry, K. E., Janes, D. M., Hunten, D. M., Kim, K. J., et al. (2004).
820 Mars' South Polar Ar Enhancement: A Tracer for South Polar Seasonal Meridional Mixing.
821 *Science*, 306(5700), 1364–1367. <https://doi.org/10.1126/science.1098496>

822 Sprague, A. L., Boynton, W. V., Kerry, K. E., Janes, D. M., Kelly, N. J., Crombie, M. K., et al. (2007).

823 Mars' atmospheric argon: Tracer for understanding Martian atmospheric circulation and
824 dynamics. *Journal of Geophysical Research: Planets*, 112(E3).
825 <https://doi.org/10.1029/2005JE002597>

826 Trainer, M. G., Wong, M. H., McConnochie, T. H., Franz, H. B., Atreya, S. K., Conrad, P. G., et al.
827 (2019). Seasonal Variations in Atmospheric Composition as Measured in Gale Crater, Mars.
828 *Journal of Geophysical Research: Planets*, 124(11), 3000–3024.
829 <https://doi.org/10.1029/2019JE006175>

830 Trokhimovskiy, A., Korablev, O., Kalinnikov, Y. K., Fedorova, A., Stepanov, A. V., Titov, A. Y., et al.
831 (2015a). Near-infrared echelle-AOTF spectrometer ACS-NIR for the ExoMars Trace Gas
832 Orbiter. In *Infrared Remote Sensing and Instrumentation XXIII* (Vol. 9608, pp. 62–70). SPIE.
833 <https://doi.org/10.1117/12.2190369>

834 Trokhimovskiy, A., Korablev, O., Ivanov, Y. S., Siniyavsky, I. I., Fedorova, A., Stepanov, A. V., et al.
835 (2015b). Middle-infrared echelle cross-dispersion spectrometer ACS-MIR for the ExoMars Trace
836 Gas Orbiter. In *Infrared Remote Sensing and Instrumentation XXIII* (Vol. 9608, pp. 55–61).
837 SPIE. <https://doi.org/10.1117/12.2190359>

838 Trokhimovskiy, A., Perevalov, V., Korablev, O., Fedorova, A. F., Olsen, K. . S., Bertaux, J.-L., et al.
839 (2020). First observation of the magnetic dipole CO₂ main isotopologue absorption band at 3.3
840 μm in the atmosphere of Mars by ACS. *Astron. Astrophys. in Press*. [https://doi.org/10.1051/0004-](https://doi.org/10.1051/0004-6361/202038134)
841 [6361/202038134](https://doi.org/10.1051/0004-6361/202038134)

842 Vandaele, A. C., Lopez-Moreno, J.-J., Patel, M. R., Bellucci, G., Daerden, F., Ristic, B., et al. (2018).
843 NOMAD, an Integrated Suite of Three Spectrometers for the ExoMars Trace Gas Mission:
844 Technical Description, Science Objectives and Expected Performance. *Space Sci. Rev.*, 214, 80.
845 <https://doi.org/10.1007/s11214-018-0517-2>

846